



HAL
open science

Some things special about NEAs: Geometric and environmental effects on the optical signatures of hydration

S. Potin, P. Beck, B. Schmitt, F. Moynier

► **To cite this version:**

S. Potin, P. Beck, B. Schmitt, F. Moynier. Some things special about NEAs: Geometric and environmental effects on the optical signatures of hydration. *Icarus*, 2019, 333, pp.415-428. 10.1016/j.icarus.2019.06.026 . hal-02415181

HAL Id: hal-02415181

<https://hal.science/hal-02415181>

Submitted on 25 Oct 2021

HAL is a multi-disciplinary open access archive for the deposit and dissemination of scientific research documents, whether they are published or not. The documents may come from teaching and research institutions in France or abroad, or from public or private research centers.

L'archive ouverte pluridisciplinaire **HAL**, est destinée au dépôt et à la diffusion de documents scientifiques de niveau recherche, publiés ou non, émanant des établissements d'enseignement et de recherche français ou étrangers, des laboratoires publics ou privés.



Distributed under a Creative Commons Attribution - NonCommercial 4.0 International License

1 *Some things special about NEAs: Geometric and environmental*
2 *effects on the optical signatures of hydration*

3

4 S. Potin¹, P.Beck^{1,2}, B. Schmitt¹, F. Moynier³

5

6 ¹Université Grenoble Alpes, CNRS, Institut de Planétologie et d'Astrophysique de
7 Grenoble (IPAG), France (414 rue de la Piscine, 38400 Saint-Martin d'Hères, France)

8 ²Institut Universitaire de France, Paris, France

9 ³Institut de Physique du Globe de Paris (IPGP) (1 Rue Jussieu, 75005 Paris, France)

10 Corresponding author: sandra.potin@univ-grenoble-alpes.fr

11

12 **ABSTRACT**

13 **Here we report on a laboratory study aiming to reproduce specificities of**
14 **near-Earth Asteroid. We study how the elevated surface temperature, their**
15 **surface roughness (rock or regolith), as well as observation geometry can affect**
16 **the absorption features detected on asteroids. For that purpose, we selected a**
17 **recent carbonaceous chondrite fall, the Mukundpura CM2 chondrite which fell in**
18 **India in June 2017. Bidirectional reflectance spectroscopy was performed to**
19 **analyze the effect of the geometrical configuration (incidence, emergence and**
20 **azimuth angle) on the measurement.** Our results show that reflectance spectra
21 obtained under warm environment (NEA-like) tends to show shallower absorption
22 bands compared to **low-temperature** conditions (MBA-like), but still detectable in our
23 experiments under laboratory timescales. Irreversible alteration of the sample because
24 of the warm environment (from room temperature to 250°C) has been detected as an

25 increase of the spectral slope and a decrease of the band depths (at 0.7 μm , 0.9 μm and
26 2.7 μm). Comparing the **meteoritic chip** and the **powdered sample**, we found that
27 **surface texture strongly affects** the shape of the reflectance spectra of meteorites and
28 thus of asteroids, **where a dust-covered surface presents deeper absorption**
29 **features. We found that all spectral parameters, such as the reflectance value,**
30 **spectral slope and possible absorption bands are affected by the geometry of**
31 **measurement. We** observed the disappearance of the 0.7 μm absorption feature at
32 phase angle **larger** than 120°, but the 3 μm band remains detectable on all measured
33 spectra.

34

35

36 1. INTRODUCTION

37

38 Many meteorite groups record the action of water at some point of their geological
39 history (Brearley 2006). Fingerprints of aqueous alteration have been identified in the
40 form of secondary minerals such as carbonates, phyllosilicates or iron oxides. Asteroids,
41 which are the astronomical counterpart of meteorites, also display evidence of aqueous
42 alteration. A first evidence, derived from visible ground-based optical observations, is
43 the presence of absorption bands at 0.7 and 0.9 μm , which can be attributed to Fe
44 bearing phyllosilicates (Vilas 2008). A more direct evidence of the presence of hydrated
45 or hydroxylated minerals at the surface of asteroids is the presence of an absorption
46 band around 3- μm . For main-belt asteroids (MBAs), observations in this spectral region
47 are only possible for the **brightest** objects (Vilas 1994; Takir and Emery 2012). Spectral
48 surveys have shown that objects with an absorption band at 0.7 μm always show the
49 presence of a 3- μm feature, but that the reciprocal is not true (Usui et al. 2019; Vilas

50 **1994).**

51

52 Two space missions are presently **orbiting** possibly volatile-rich near-Earth
53 asteroids (NEAs): Hayabusa-2 (**Kitazato et al. 2019**) and **OSIRIS-Rex (Hamilton et al.**
54 **2019)**. While hydration seems to be a general process among the **MBAs** population
55 (Fornasier et al. 2014), evidence of hydrated near-Earth asteroid is scarce (**Rivkin et al.**
56 **2002)**. **Rivkin and DeMeo (2018)** calculated the theoretical amount of hydrated NEAs
57 according to their spectral group and found $17 \pm 3\%$ for the Ch-group and $43 \pm 6\%$
58 corresponding to C-complex bodies. However, observations **from Stuart and Binzel**
59 **(2004) and Carry et al. (2016)** resulted in the statistics of $6 \pm 3\%$ of NEAs showing
60 signs of Ch asteroids, and $16 \pm 7\%$ showing signatures of C-complex asteroids. While
61 NEAs are certainly more accessible for sample-return purposes, it is not known today
62 whether they experienced specific, or more intense, geological processes when
63 compared to main-belt asteroids. First, it has been shown that the orbital evolution of
64 the NEA (101955) Bennu, the target of **the OSIRIS-REx** mission, could have led to a
65 significant heating of the surface (over 500 K (Delbo and Michel 2011)) by absorption of
66 solar radiation, which is much higher than the surface temperature experienced in the
67 main-belt (Schorghofer 2008). Second, many NEAs seem to exhibit a rubble pile
68 structure. These rubble-pile asteroids are interpreted as re-agglomerated fragments of a
69 prior object that was catastrophically destroyed following a hypervelocity collision
70 (Michel, Benz, and Richardson 2003, 2004). Last, small NEAs visited by space missions
71 appear devoid of a significant amount of **dust-like** regolith (Fujiwara et al. 2006), which
72 is at odd with larger objects visited by space missions (Veveřka et al. 1997).

73

74 In this article, we investigate how the environment of NEAs and the observations

75 themselves can influence the signatures of aqueous alteration. For that purpose, we
76 selected a freshly fallen aqueously altered meteorite, the Mukundpura CM2 chondrite.
77 The impact of thermal processing on the infrared signature has been studied in situ
78 using a high-temperature, high-vacuum reflectance cell. The effect of observation
79 geometry and the impact of surface texture (comparison **between** rock and **dust no**
80 **larger than a few hundreds of microns**) have been investigated using a custom-made
81 reflectance-goniometer (Potin et al. 2018).

82

83 **2. Sample and methods**

84 **2.1 Meteorite sample**

85

86 The Mukundpura meteorite fell in India on June 6, 2017 (Tripathi, Dixit, and
87 Bhandari 2018) and was immediately collected by the authorities, reducing the risk of
88 post-fall alteration. The first petrographic observations of the newly fallen meteorite
89 were performed using a Zeiss polarizing microscope and electron microprobe (Ray and
90 Shukla 2018) and characterized the meteorite as belonging to the CM group.

91

92 Mukundpura presents a dark matrix and several millimeter-size bright inclusions
93 (see Figure 1). The sample used in this study was taken from the exterior of the whole
94 meteorite and thus showed a smooth fusion crust **on one of its side**. Only the interior of
95 the **sample, the side opposite to the crust**, was studied in reflectance spectroscopy.



96

97 **Figure 1: Picture of the Mukundpura meteorite sample used in this study (interior**
98 **side showing).**

99

100 This sample was first studied as a **chip of the meteorite**, then powdered to
101 investigate the effect of texture on the reflectance spectra.

102

103 2.2 Bidirectional reflectance spectroscopy

104 2.2.1 Definition and methods for bidirectional reflectance spectroscopy
105 under fixed geometry, room temperature and atmospheric pressure.

106

107 Reflectance spectroscopy studies are conducted using the custom-made
108 bidirectional reflectance goniometers SHINE (**SpectropHotometer with variable**
109 **INcidence and Emergence**) (Brissaud et al. 2004) and SHADOWS
110 (**Spectrophotometer with cHanging Angles for the Detection Of Weak Signals**)
111 (Potin et al. 2018), whose methods of measurement are quite similar. The goniometer
112 illuminates the sample with a monochromatic light between 340 nm and 5000 nm and
113 under a specific direction (incidence angle). Table 1 summarizes the different spectral
114 resolutions over the whole spectral range.

115

116 **Table 1: Spectral resolution of the reflectance spectrum**

| Spectral range | Spectral resolution |
|-------------------|---------------------|
| 400 nm – 679 nm | 4.85 nm – 4.75 nm |
| 680 nm – 1499 nm | 9.71 nm – 9.38 nm |
| 1500 nm – 2999 nm | 19.42 nm – 18.73 nm |
| 3000 nm – 5000 nm | 38.84 nm – 38.44 nm |

117

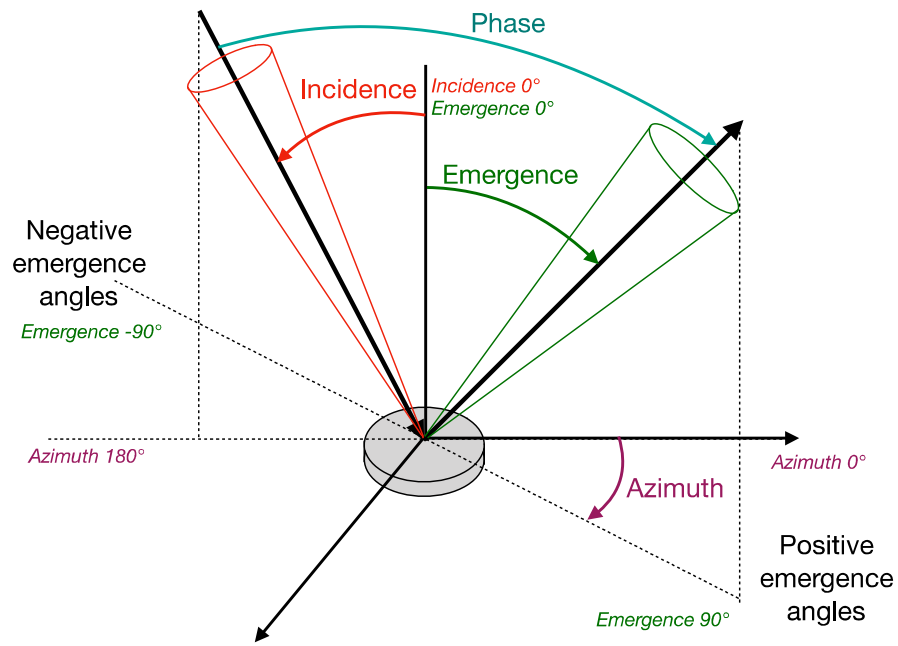
118

119 The reflected light is measured under fixed values of emergence and azimuth angles.

120 All three parameters, incidence, emergence and azimuth angles, constitute the

121 geometrical configuration under which the spectra will be recorded. Figure 2 presents a

122 schematic view of the reflectance measurement and the different angles involved.



123

124 **Figure 2: Schematic definition of the geometrical configuration, incidence,**
 125 **emergence and azimuth angles, for the reflectance spectroscopy. Picture from**
 126 **Potin et al. (2018).**

127

128 Nominal configuration for a “single spectrum” reflectance spectroscopy study
 129 consists of a nadir illumination (incidence angle of 0°) and an emergence angle of 30° in
 130 the principal plane (azimuth 0°). The angular resolutions are $\pm 2.9^\circ$ for the incidence
 131 angle and $\pm 2.05^\circ$ for the emergence and azimuth angles.

132

133 2.2.2 Reflectance spectroscopy under asteroidal conditions.

134

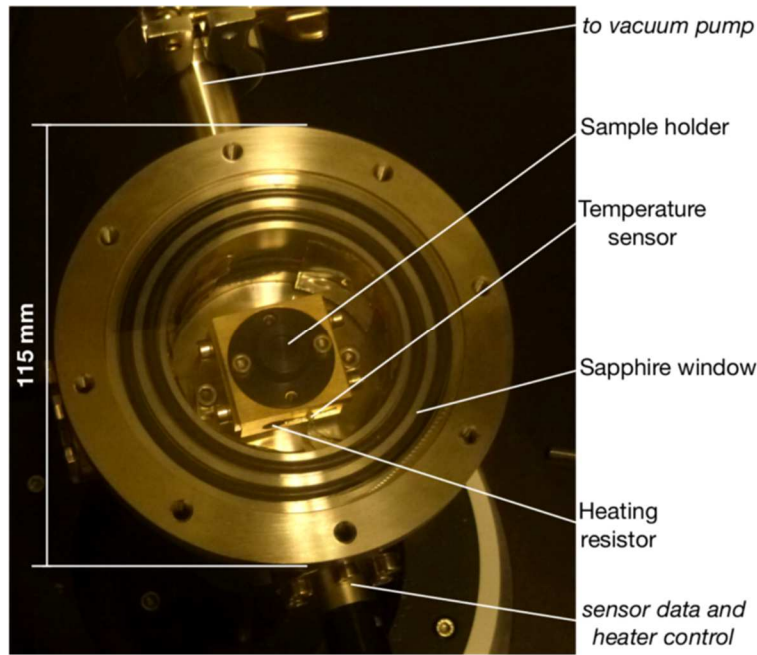
135 **Low-temperature** reflectance spectra are acquired using SHINE coupled with
 136 the double environmental chamber CarboN-IR (Beck et al. 2015; Grisolle et al. 2014).
 137 The outer cell is put under vacuum while gaseous nitrogen is injected inside the inner
 138 cell to increase the thermal exchanges and ensure thermalization of the sample. This

139 technique reduces the thermal gradient inside the meteorite but needs two sapphire
140 windows to close the outer and inner cells. The light passing through these two
141 windows creates reflections between the sample and the inner cell window, but also
142 between the windows themselves. The small absorption of the sapphire added to the
143 multiples reflections reduce the contrast of reflectance measured on a sample. To
144 evaluate the effect of the two windows on the measurement, reflectance spectra of a
145 calibration target were acquired, with and without the sapphire windows. Using these
146 spectra, the effects of the windows have been removed from the meteorite data. The
147 spectra were acquired, with a nadir illumination and emergence angle of 30°, from 80K
148 to room temperature 290K every 10K, and from 400 nm to 1000 nm with a 10 nm
149 spectral sampling.

150

151 Reflectance spectroscopy at high temperature can be conducted with SHADOWS
152 using a heating vacuum cell, nicknamed MIRAGE (**Mesures en InfraRouge sous**
153 **Atmosphère Gazeuse et Etuvée**) (see Figure 3).

154



155

156

Figure 3: Annotated picture of the MIRAGE cell.

157

158 This cell only needs one sapphire window, and the presence of reflections
159 between the window and the sample has already been investigated and corrected
160 through the work on the SERAC cell (**Spectroscopie En Réflexion sous Atmosphère**
161 **Contrôlée**) (Pommerol et al. 2009). Other sources of error need to be taken into account
162 with MIRAGE, but were previously unknown on SERAC, due to the difference between
163 the illumination methods of the two setups. To remove all these effects, reflectance
164 spectra of Mukundpura were acquired with and without the sapphire window, and used
165 to correct the instrumental biases due to the cell on all the acquisitions. The spectra
166 were acquired from 360 nm to 1200 nm every 10 nm in order to analyze the shape of
167 the 700 nm and 900 nm bands. Acquisitions are set from room temperature (294 K) to
168 510K every 20K during the increase of temperature, and from 490K to room
169 temperature every 40K when the cell is cooling down. The illumination is fixed at nadir,
170 and the observation at 30°.

171

172 2.2.3 Bidirectional Reflectance Distribution Function (BRDF)

173

174 To simulate observations from a spacecraft orbiting its target or from a ground-
175 based observatory, one has to take into account the scattering geometry of the system:
176 the angle of the light illuminating the surface, as well as the angle from which the spectra
177 are acquired. In the laboratory, bidirectional reflectance spectra were acquired with
178 SHADOWS for 70 different geometrical configurations: incidence, emergence and
179 azimuth angles. The incidence angle was set from nadir to grazing illumination (0° to
180 60° with a 20° step), and for each incidence, spectra were acquired at several
181 measurement angles from -70° to 70° , corresponding to grazing emergence respectively
182 in the backscattering and forward scattering directions in the principal plane, with a 10°
183 step. To analyze the lateral scattering of the sample, spectra at incidence 20° with the
184 same list of emergence angles were taken with a 30° azimuth angle outside the principal
185 plane. The SHADOWS goniometer cannot measure light reflected at a phase angle lower
186 than 5° so opposition spectra are absent from the dataset. The spectral resolution is
187 identical to the resolutions displayed in Table 1. The angular resolutions are $\pm 2.9^\circ$ for
188 the incidence angle and $\pm 2.05^\circ$ for the emergence and azimuth angles.

189

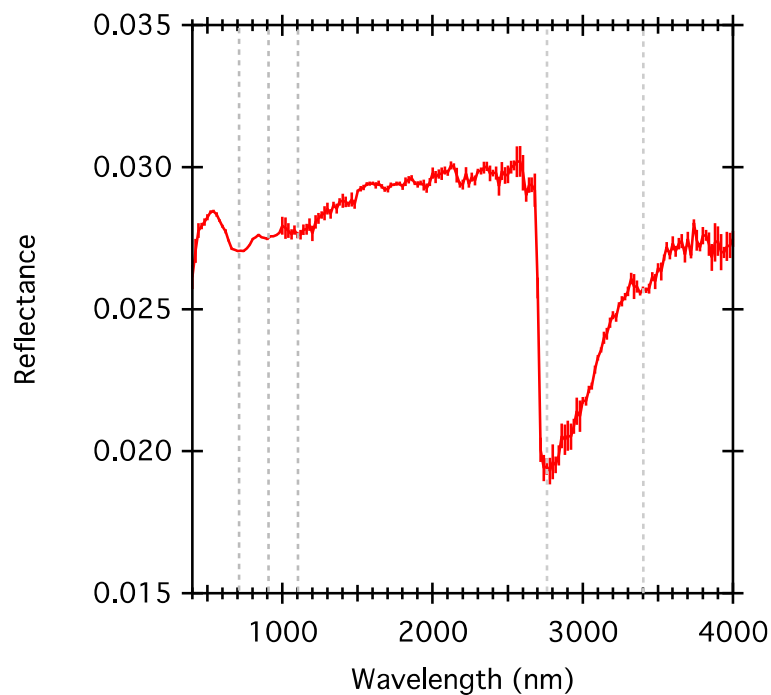
190 The series of spectra has been first acquired on the **chip**. The studied surface
191 originated from a broken piece of a larger sample and therefore was not **horizontal**
192 **when placed on the goniometer (tilt of about 5°)**. This was taken into account during
193 the analysis and photometric corrections were applied to the data. The same set of
194 reflectance spectra have been acquired after manual grinding of the meteorite, to
195 compare the photometric and spectral variations due to surface texture.

196

197 3. Reflectance spectroscopy

198 3.1 Spectral features of the Mukundpura CM chondrite

199 The reflectance spectrum of the powdered meteorite is displayed on Figure 4. A
200 first series of spectra was acquired under vacuum, starting at room temperature then at
201 60°C. There was no evidence of degassing of the sample.



202

203 **Figure 4: Reflectance spectrum of the Mukundpura meteorite (powder) with a**
204 **nadir illumination and an emergence angle of 30°. The grey dotted lines mark the**
205 **position of the typical CM absorption bands at 700 nm, 900 nm, 1100 nm, 2760 nm**
206 **and 3400 nm.**

207

208 The reflectance spectrum shows all characteristics of CM chondrites (Cloutis, Hudon,
209 et al. 2011): (1) a low reflectance value, less than 3% over the whole spectral range, (2)
210 the Fe³⁺-Fe²⁺ charge-transfer band at 700 nm (Tomeoka, Mcsween, and Buseck 1989),

211 (3) the Fe²⁺ crystal field transition bands at 900 and 1100 nm, (4) organics features at
212 3400 nm and (5) the -OH stretching band at 2750 nm related to the presence of Mg-OH
213 bearing phyllosilicates.

214

215 The beginning of a strong UV absorption feature is visible shortwards of 500 nm,
216 though it is not possible to analyze this band with the current data starting at 400 nm.
217 This absorption feature is likely due to metal-O charge transfer (Cloutis et al. 2008).

218

219 The detection of both the iron features (700 nm and 900 nm) and the Mg-rich
220 phyllosilicates band at 2750 nm indicates an extensive aqueous alteration of the
221 meteorite on the parent body (Takir et al. 2013; Beck et al. 2010).

222

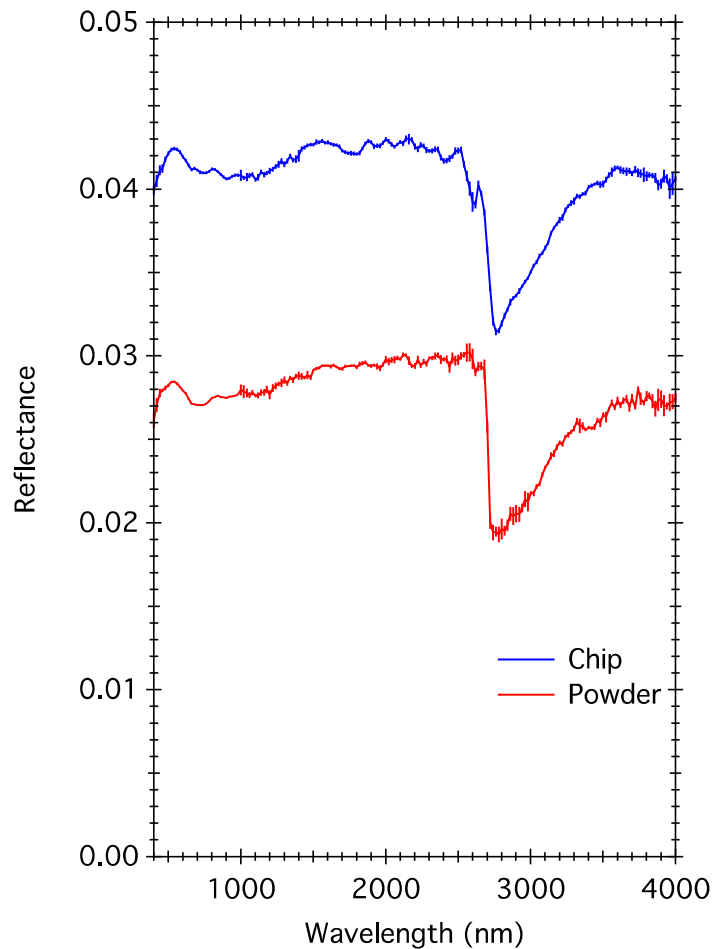
223 3.2 Assessing the impact of regolithisation: comparison between the **chip** and
224 the powdered sample

225

226 Reflectance spectroscopy of the **meteoritic chip** was conducted under the same
227 geometrical configuration as the powder. The sample was placed on its fusion crust on
228 the sample holder so that the studied surface was revealing the interior of the meteorite.

229 Both spectra are presented in Figure 5.

230



231

232 **Figure 5: Reflectance spectra of the raw meteorite (blue) and after manual**
 233 **powdering (red).**

234

235 The major difference between the two sets of spectra is the reflectance value of
 236 the continuum, around 4.2% in the case of the raw meteorite and around 2.8% for the
 237 powder. This behavior is distinct from the “standard” behavior observed for pure
 238 material when the grain size is decreased, which is to observe an increase in reflectance
 239 with decreasing grain size (Pommerol and Schmitt 2008b). Several possible
 240 explanations emerge. The first explanation is related to petrography: the surface of the
 241 raw meteorite is heterogeneous due to the presence of mm-sized chondrules and bright
 242 inclusions, while the powder has all the elements finely mixed into a rather

243 homogeneous volume. Opaques “hidden” beneath the surface will be more visible in the
244 powder spectra, lowering the global amount of reflected light. The model developed by
245 Hapke (1981) states that the reflectance of an intimate mixtures depends on the viewing
246 geometry and properties of the particles in the mixtures such as single scattering albedo,
247 diameters, porosity and mass fraction. The spectra of mixtures composed of materials
248 with contrasted absorption properties will depend on the style of the mixture. In the
249 case of a spatial mixture of two spectral endmembers, the resulting spectrum is a linear
250 mix of the endmember spectra, weighted by their surface area. The spectra of the raw
251 meteorite, where the size of the bright and dark patches are less than 1 mm² can be
252 interpreted by a linear mixture of the bright and dark endmembers. When powdering
253 the meteorite, the style of mixture between the dark and bright materials will change,
254 since it will become an intimate mixture. In that case, mixtures are expected to be linear
255 in single scattering albedo space, and therefore the mixture of the spectra becomes
256 highly non-linear. For the same amount of bright and dark material, the intimate
257 mixture (powder) will be darker than in the case of a geographic mixture (**chip**)
258 (Pommerol and Schmitt 2008b).

259

260 The second explanation could be the difference of porosity between the two
261 samples. Theory and laboratory measurements agree that increasing the porosity of a
262 sample lowers the general reflectance (Hapke 2008; Cloutis et al. 2018; Shepard and
263 Helfenstein 2011; Cloutis, Hiroi, et al. 2011) The presence of bright inclusions coupled
264 with the differences in both grain size and porosity between the samples can explain the
265 higher reflectance of the raw meteorite.

266

267 Both samples present the same absorption features, but with different band

268 depth and broadness. Relative band depths are calculated considering a linear
 269 continuum between the two inflexion points of the bands and using the following
 270 formula:

271

$$272 \quad BD = 1 - \frac{R_{band}^c}{R_{continuum}^c}$$

273

274 where c is the central wavelength of the absorption band, R_{band}^c and $R_{continuum}^c$ are
 275 respectively the measured reflectance of the sample and the interpolated reflectance of
 276 the continuum at wavelength c . The depth of the UV absorption band is calculated as the
 277 ratio between the reflectance measured at 540 nm and 400 nm:

278

$$279 \quad UV \text{ ratio} = \frac{R^{540nm}}{R^{400m}}$$

280

281 Table 2 presents the calculated band depths of the UV absorption, the Fe²⁺ 700
 282 nm band, the phyllosilicates 3 μm feature and the organics band around 3400 nm.

283

284 **Table 2: Band depths of the Vis-NIR absorption features and UV ratio calculated**
 285 **for the chip and powdered samples.**

| | UV ratio | 700 nm band | 3 μm band | Organics |
|--------------------|-----------------|-----------------|-----------------|-----------------|
| Chip | 1.0618 ± 0.0074 | 0.0139 ± 0.0037 | 0.1992 ± 0.0090 | 0.0080 ± 0.0061 |
| Powdered meteorite | 1.089 ± 0.018 | 0.0306 ± 0.0017 | 0.3252 ± 0.0009 | 0.0281 ± 0.0088 |

286

287 We found that grinding of the sample affects the absorption features, resulting in a
 288 deepening of the bands. Again, the size of the grains will affect the depth of the

289 absorption features, following the general trend where band depth increases with
290 increasing grain size. It should be noted that all absorption bands are detectable in both
291 reflectance spectra. This implies that even in the absence of a well developed **fine-**
292 **grained** regolith, as seems to be the case for some near-earth objects (Benner et al.
293 2008; Hasegawa et al. 2008), the water-related features should be detectable. In order
294 words, the lack of **dust-size** regolith does not explain the scarcity of water-related
295 absorption signatures among the NEAs population.

296

297 **4 Effects of temperature on the optical absorptions**

298

299 Several processes may warm the surface of small bodies, NEAs included. First, the
300 initial decay of extinct radionuclide such as ^{26}Al , could have been strong enough to heat
301 up and differentiate small bodies (Grimm and Mccween 1993,1989; Mahan et al. 2018),
302 but this process was not efficient for km-size objects (Ghosh et al. 2006). Secondly,
303 impacts can generate enough heat to locally metamorphose or even melt the surface
304 (Bland et al. 2014), though the models cannot describe a global increase of the
305 temperature of the object. This is consistent with some of the heated meteorites
306 showing foliation or shock-induced deformations (**Nakamura 2006**). The initial
307 accretion process is based on low energy impacts and thus can be disregarded as a
308 source of heating for the small bodies (**Nakamura 2005**). Then, electromagnetic
309 induction due to solar winds during the early T Tauri phase can induce enough heat to
310 alter the mineralogy of asteroids. But as the solar winds usually occur on the poles of the
311 stars, they are unlikely to have produced enough heat in the mid-plane where the small
312 bodies are concentrated (Mahan et al. 2018). Last but not least, the relatively close
313 distance between the Sun and the NEAs over their lifetime induces an elevated sunlight

314 flux on the surface, and so warming up the small body. This process depends on albedo,
315 surface roughness and thermal inertia. An elevated thermal inertia will reduce the
316 difference of temperature between the direct sub-solar surface (strongly heated) and
317 the rest of the body (rather cool) and the rotation period, **as well as the pole position**,
318 of the asteroid will also have an impact on the temperature at the surface. In the case of
319 a slow-rotating body **or an asteroid oriented so that its rotation axis is near the**
320 **orbital plane with a pole facing toward the Sun**, the sub-solar point will accumulate a
321 lot of heat and will reach higher temperatures than the night-side, and the whole surface
322 of the body will present a wide range of temperatures that strongly vary with time. On
323 the contrary, fast-rotating asteroids, **or with their rotation axis almost perpendicular**
324 **to the orbital plane**, will present a rather homogeneous and moderate temperature on
325 their surface. For example, according to models, (101955) Bennu could have undergone
326 temperatures as high as 500K (Delbo and Michel 2011), while other NEAs could have
327 experienced temperatures over 1500K during a close approach to the Sun (Marchi et al.
328 2009). Note however that Dunn et al. (2013) calculated that the temperature of 72 NEAs
329 is distributed between 143 and 300K.

330

331 Reflectance spectra of asteroids can be affected by surface temperature, an effect
332 which was studied for S-type asteroids and ordinary chondrites, but which is much less
333 known for C-type asteroids. In this section, we present the spectral variations of the
334 powdered Mukundpura meteorite under a wide range of environmental conditions,
335 from cryogenic to high temperature. We focus on the iron features in the visible range.

336

337 To characterize the spectral variations across changes in temperature, the
338 reflectance spectra are adjusted using a linear continuum and three modified Gaussian

339 profiles (Sunshine, Pieters, and Pratt 1990) representing the UV, 700 nm and 900 nm
340 absorption bands. The modified Gaussian model (MGM) includes a correction factor
341 acting on the symmetry of the left and right wings of the profile. Its value can be fixed
342 empirically. The least residual errors were achieved with a correction factor of 1.12. For
343 each MGM, so for each absorption feature, the amplitude, band position and full width at
344 half maximum (FWHM) are set as free parameters. The resulting model is as follow:

345

$$346 \quad R(\lambda) = A\lambda + B + MGM(\lambda, a_{UV}, p_{UV}, \sigma_{UV}) + MGM(\lambda, a_{700nm}, p_{700nm}, \sigma_{700nm})$$
$$347 \quad + MGM(\lambda, a_{900nm}, p_{900nm}, \sigma_{900nm})$$

348

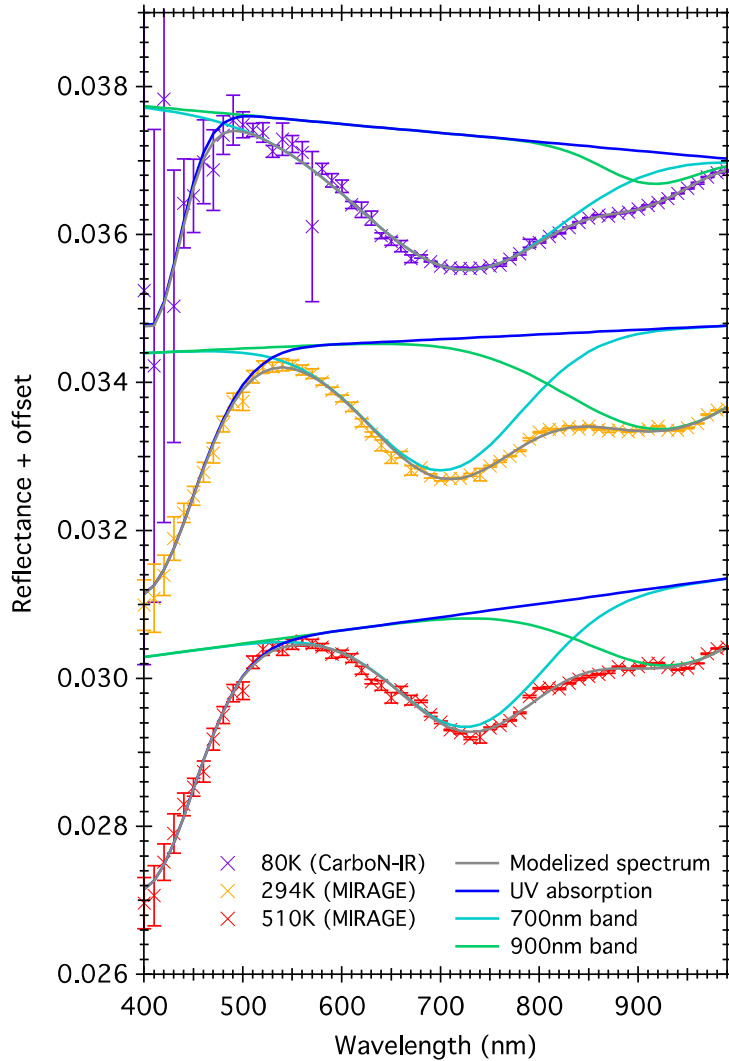
349 with $R(\lambda)$ the calculated reflectance at the wavelength λ , A and B respectively the slope
350 and offset of the continuum, and a_x, p_x and σ_x the amplitude, position and FWHM
351 (linked to σ) of the band X. The model parameters for the UV absorption may differ from
352 reality, as the data cover less than half the band.

353

354 4.1 Variations from cryogenic to high temperatures.

355

356 In order to highlight the effect of temperature on the sample, Figure 6 presents a
357 comparison between the extreme spectra, obtained at 80 K and 510 K, and the
358 acquisition at room temperature.



359

360 **Figure 6: Comparison between the reflectance spectra of the powdered**
 361 **Mukundpura meteorite acquired at 80K (purple), room temperature (orange) and**
 362 **510K (red). The modeled spectra (grey) and the different modeled absorption**
 363 **bands, UV (navy blue), 700 nm (blue), and 900nm (green) are also presented. An**
 364 **offset of +0.003 and -0.003 has been added respectively to the 80K and 510K**
 365 **spectra.**

366

367 In Figure 6, subtle variations of the spectra related to temperature can be
 368 observed. The fit parameters for each spectrum are compared in Table 3.

369

| | 80K | 294K | 510K |
|-------------------------------------|-------------------------|------------------------|------------------------|
| Continuum slope (nm ⁻¹) | -1.210.10 ⁻⁶ | 6.299.10 ⁻⁷ | 1.797.10 ⁻⁶ |
| Continuum offset | 0.0352 | 0.0341 | 0.0326 |
| BD _{700nm} (%) | 0.183 | 0.177 | 0.153 |
| P _{700nm} (nm) | 710 | 702 | 730 |
| FWHM _{700 nm} (nm) | 330 | 252 | 239 |
| BD _{900nm} (%) | 0.043 | 0.136 | 0.107 |
| P _{900nm} (nm) | 910 | 926 | 940 |
| FWHM _{900 nm} (nm) | 167 | 327 | 298 |
| BD _{UV} (%) | 0.298 | 0.327 | 0.314 |
| P _{UV} (nm) | 404 | 394 | 396 |
| FWHM _{UV} (nm) | 105 | 176 | 171 |
| Reflectance max | 0.0344 | 0.0342 | 0.0334 |
| Position of the max (nm) | 491 | 539 | 560 |

370 **Table 3: Parameters of the modeled spectra at each temperature.**

371

372 The increase of temperature induces a modification of the continuum slope, as
373 seen by the spectrum at 80K having a negative (blue) slope, while the spectra acquired
374 at room temperature and 510K present a positive (red) slope. A decrease of reflectance
375 of the continuum is observed at 510K, representing 7.4% relative to the initial value at
376 80K. Variations of the absorption features as well as the continuum induce an apparent
377 displacement and decrease of the maximum of reflectance, from 0.0344 of reflectance at
378 491 nm in the spectrum acquired at 80K, to a reflectance of 0.0334 at 560 nm for the
379 spectrum at 510K. The reflectance maximum also decreases with increasing

380 temperature, losing 0.001 of reflectance between the two extreme spectra.

381

382 In the case of the low temperature measurements, a blue shift of nearly 20 nm of
383 the position of the 700 nm band can be observed when compared to the high
384 temperature measurement. The band gets broader and deeper, as the FWHM gains
385 around 97 nm and the depth increases by a factor 1.2. It is interesting to note that
386 opposite effects occur in the case of the 900 nm band, except for the position: with
387 decreasing temperature, the band is shifted by 30 nm towards shorter wavelengths, the
388 band depth is reduced by a factor 2.5 and its FWHM is reduced by approximately
389 130nm.

390

391 Fe-related absorptions can be expected to be sensitive to temperature (Hinrichs and
392 Lucey 2002). The 700 nm feature in CM chondrites is interpreted by Fe²⁺-Fe³⁺ charge
393 transfer (Fe²⁺+Fe³⁺ ->Fe³⁺+Fe²⁺) within a phyllosilicate structure. Charge transfer bands
394 in -OH bearing silicates generally display an increase of their intensity under low-
395 temperature, as observed by Smith (1977). As measured in transmission (absorbance),
396 the intensity of the Fe²⁺-Fe³⁺ charge transfer band of chlorite and biotite has been
397 measured to increase by a factor of 2 when cooling the sample to liquid helium
398 temperature (5.5 K), and by about 25 % when cooling the sample to 80K. This effect was
399 interpreted by a depopulation of one or more electronic levels close to the ground state
400 of the Fe²⁺+Fe³⁺ ->Fe³⁺+Fe²⁺ transition (Smith 1977). While our lowest temperature
401 measurements are not as low as liquid helium, they are cold enough to induce a
402 significant increase in the depth of the 0.7 μm feature. Note that a broadening of the
403 700nm band was also observed **by Smith (1977)** study, which could explain the change
404 in the position of the visible maxima from around 539 nm (room temperature) to 491

405 nm (80 K), when added to a possible displacement and broadening of the UV absorption.

406

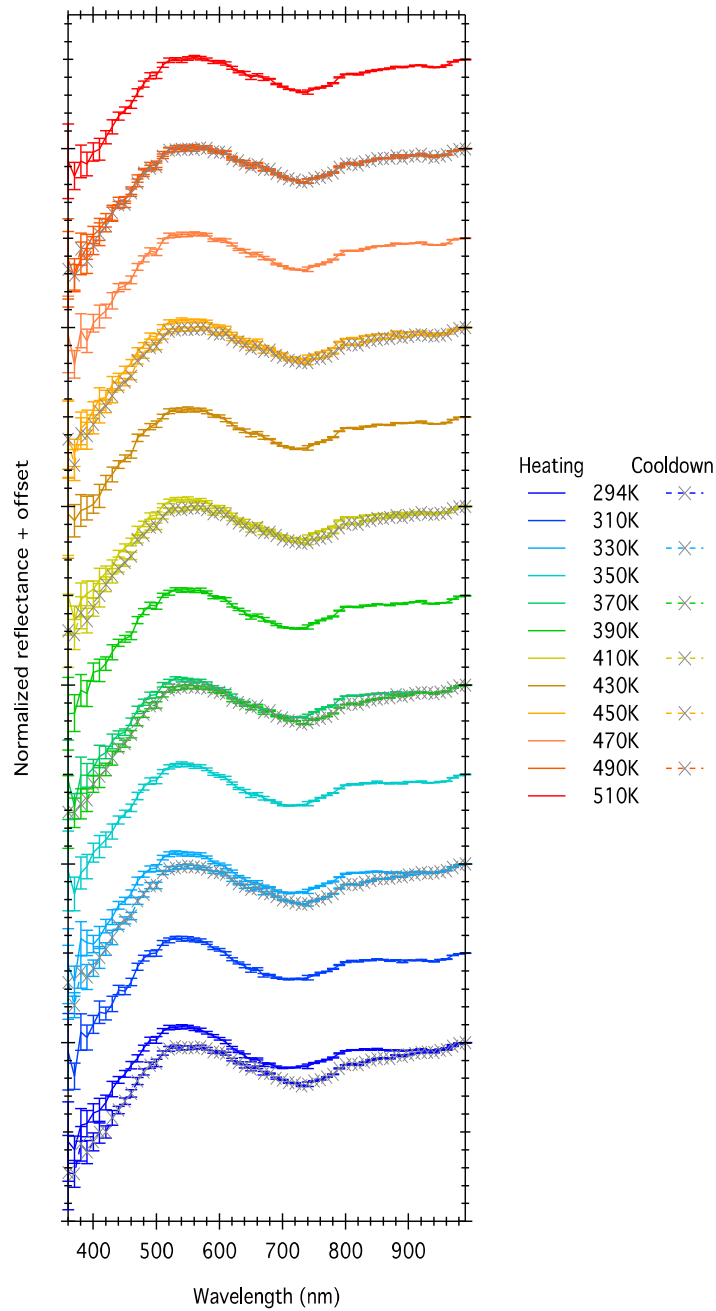
407 4.2 Irreversible alteration at high temperatures

408 Reflectance spectra of Mukundpura were recorded during a high temperature

409 experiment. Spectra were acquired during a heating and cooling cycle of the sample and

410 are presented in Figure 7.

411



412

413 **Figure 7: Normalized reflectance spectra of the powdered Mukundpura meteorite**
 414 **acquired during the increase of temperature from 294K to 510K (solid lines) and**
 415 **during cooling (dashed lined and grey markers). The different offsets have been**
 416 **added for clarity but are identical for spectra acquired at the same temperature.**

417

418

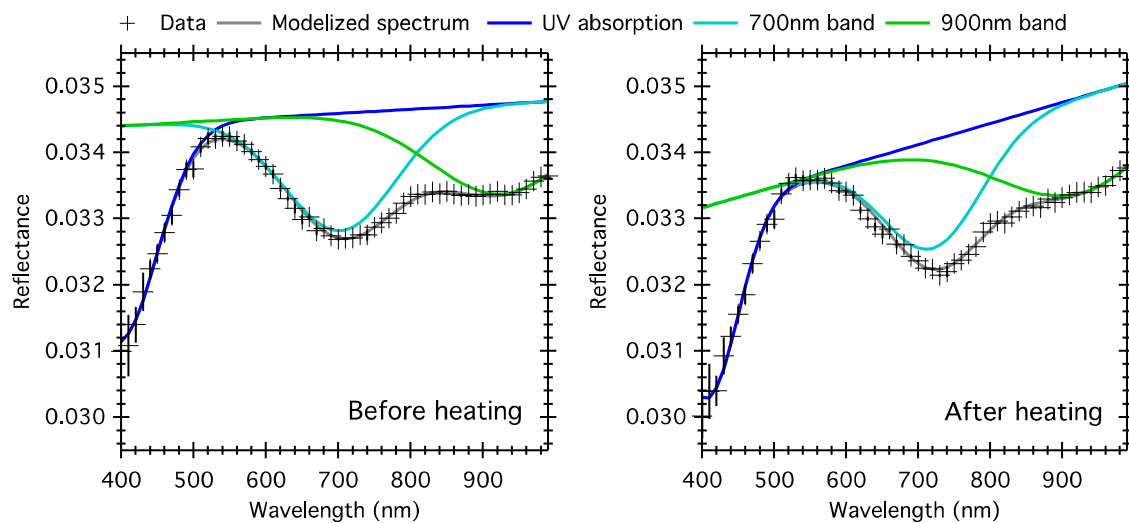
The high temperature experiments reveal irreversible alterations of the sample, as seen when comparing the two spectra taken at 294K, at the beginning and at the end

419 of the experiment. The oxidation of the sample by ambient air is not relevant in our
420 measurements as they were performed under secondary vacuum.

421

422 The difference between the two spectra is a combination of variations in the
423 continuum of the spectrum and in the 3 detectable absorptions bands. The differences
424 involve an apparent reddening of the sample as the spectrum acquired after heating
425 presents a stronger spectral slope compared to the initial measurement, an apparent
426 displacement of the 700 nm band to longer wavelengths, and both a shift and decrease
427 of the reflectance maximum around 550nm. The whole series of spectra are adjusted
428 using the model described above. Resulting modeled spectra of the first and last
429 measurements of the experiment are presented in Figure 8.

430

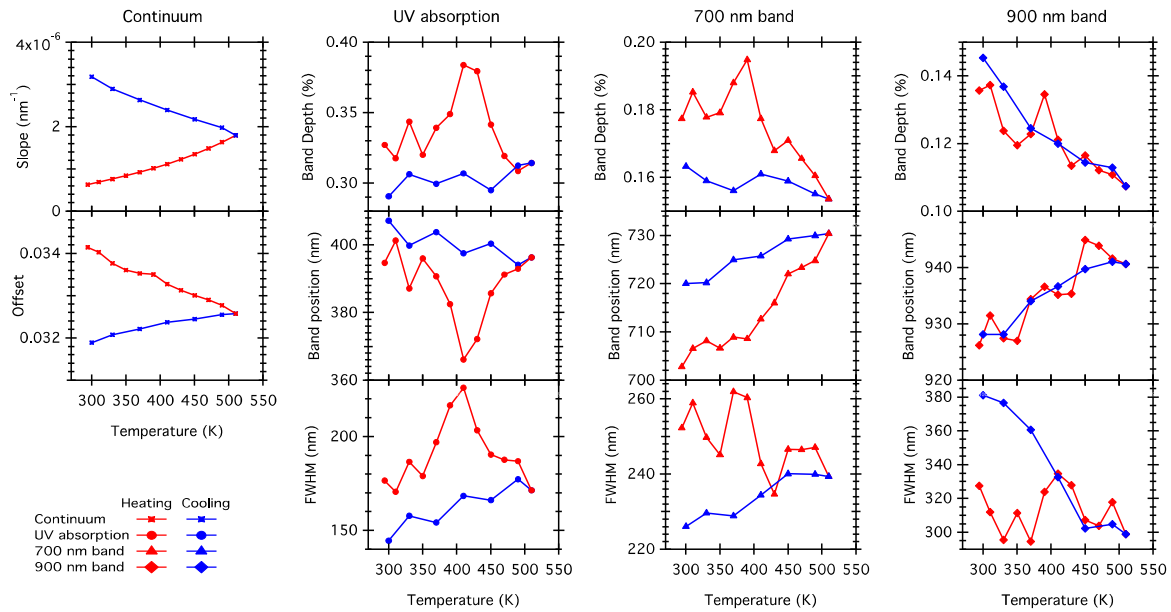


431

432 **Figure 8: Reflectance spectra of powdered Mukundpura meteorite at room**
433 **temperature (294 K) before (left) and after (right) warming to 510 K, as well as**
434 **the MGM fit to the data (Navy blue: continuum and UV absorption. Blue:**
435 **continuum and 700nm band, Green: continuum and 900nm band)**

436

437 The variation the model parameters calculated for the spectra measured during
 438 the heating and cooling cycle, is presented in Figure 9.



439
 440 **Figure 9: Variations of the continuum and absorption bands during the heating**
 441 **(red) and cooling (blue) cycle of the sample.**

442
 443 Based on this analysis, the continuum slope and all the three absorption features
 444 show an irreversible alteration due to temperature. In the case of Mukundpura, the
 445 temperature cycle up to 510 K and down leads to an increase of the continuum slope,
 446 from $6.30 \cdot 10^{-7} \text{ nm}^{-1}$ to $3.18 \cdot 10^{-6} \text{ nm}^{-1}$ after the thermal ramp, coupled with a decrease of
 447 the general reflectance level represented by the continuum offset, from 0.0341 to
 448 0.0319.

449
 450 With increasing temperature, the 700 nm band first increases and then decreases
 451 in amplitude, while getting narrower and shifting towards longer wavelengths. During
 452 cooling, the amplitude of this feature only marginally changes and returns to a value
 453 only slightly lower than prior heating (0.163% against 0.177%). Upon heating, the

454 position of the 700 nm band changes significantly. When heating to 520 K the maxima of
455 absorption shifts from 703 to 730 nm, and upon cooling it returns to a value of 720 nm.
456 The position of the 700 nm band is thus not reversible upon heating. This effect could be
457 interpreted by the occurrence of redox process (Fe^{3+} reduction of Fe^{2+} oxidation) within
458 the phyllosilicates occurring upon heating, since the oxygen fugacity is sensitive to
459 temperature.

460

461 The 900 nm also reveals some variability with temperature but in a different way
462 than the 700 nm band. The amplitude of the band decreases upon heating from 0.130%
463 to 0.107% while the position shifts to higher wavelength by about 15 nm (from 926 to
464 941 nm). Unlike the 700 nm band, these changes are reversible when returning to
465 ambient temperature (except the FWHM which significantly increases upon cooling).
466 The 900 nm band is interpreted as a crystal field band, which are known to shift,
467 broaden and change in intensity with temperature (Burns 1993), in a reversible manner.

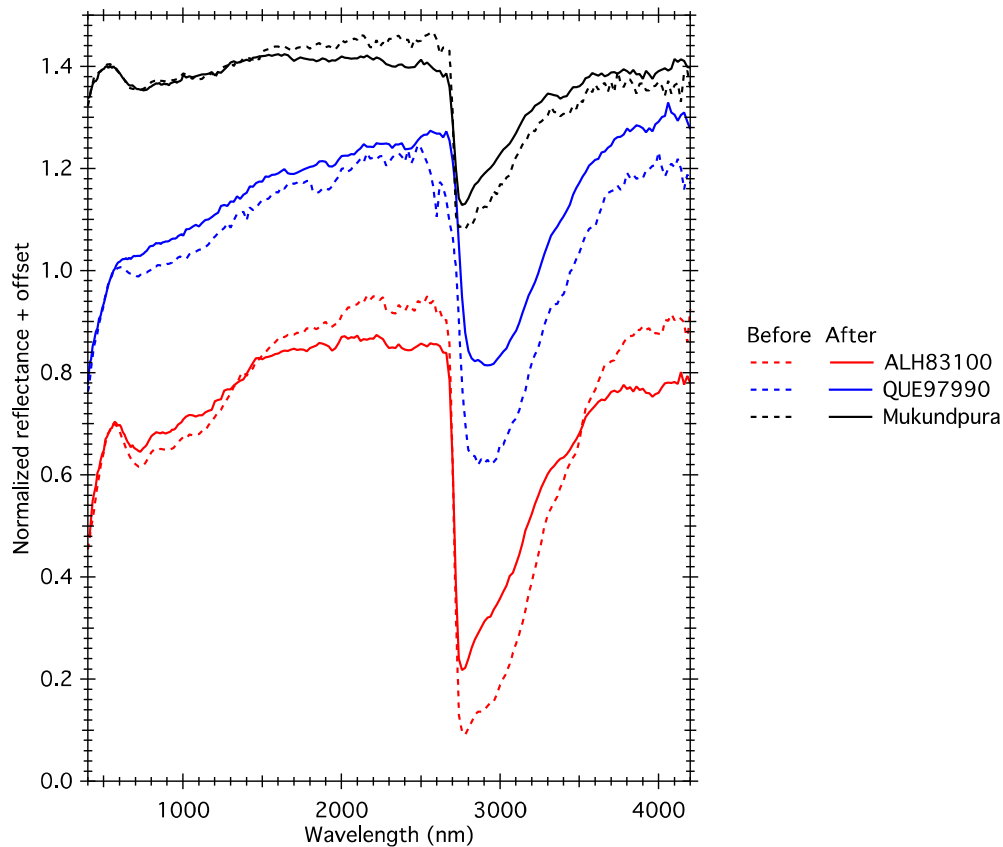
468

469 The combined spectral variations due to temperature induce the apparent
470 displacement of the maximum of reflectance from 530 nm to 558 nm at the end of the
471 thermal cycle. The value of the maximum reflectance has been altered as well, slightly
472 decreasing from 0.0342 to 0.0335 after the experiment.

473

474 Irreversible alterations also occurred outside the visible spectral range. To
475 compare the different effects observed, the same thermal cycle was imposed on 2 other
476 CM chondrites. Figure 10 presents the reflectance spectra over the whole spectral range
477 of the 3 samples before and after the experiment. As the spectroscopy measurements on
478 the whole spectral range was conducted after the temperature ramp, the samples were

479 prepared into another sample holder, the surfaces have slightly changed between the
480 two experiments. To remove this photometry effect, the spectra are normalized at
481 560nm.



482

483 **Figure 10: Normalized reflectance spectra of the CM chondrites ALH83100 (red),**
484 **QUE97990 (blue) and Mukundpura (black) acquired before (dotted line) and after**
485 **(solid line) a thermal cycle at 520 K. The spectra are normalized at 560 nm and**
486 **offseted for clarity, -0.3 and +0.4 respectively for ALH83100 and Mukundpura. All**
487 **samples were manually powdered before the experiment.**

488

489 The thermal experiment resulted in another alteration, this time of the 3 μ m
490 absorption band. Table 4 presents the band depth and width of the 3 μ m band before and
491 after the thermal cycle for the 3 chondrites.

492 **Table 4: Band depth and FWHM of the 3 μ m band before and after the thermal**
 493 **cycle for the 3 CM chondrites.**

| | Band depth (%) | | FWHM (nm) | |
|------------|------------------|------------------|-----------|-------|
| | Before | After | Before | After |
| Mukundpura | 32.52 \pm 0.08 | 26.17 \pm 0.30 | 410 | 370 |
| ALH83100 | 66.86 \pm 0.39 | 54.27 \pm 0.17 | 560 | 490 |
| QUE97990 | 49.43 \pm 0.57 | 35.21 \pm 0.15 | 650 | 530 |

494

495 For each sample, the thermal heating reduces both the depth and width of the
 496 band. A faint displacement of the band is also detected, which can be explained by the
 497 faster reduction of one of the component of the band compared to the others. The
 498 alteration of the 3 μ m band can be due to the release of the absorbed water molecules,
 499 and the water contained in (oxy)hydroxide minerals (Garenne et al. 2014).

500

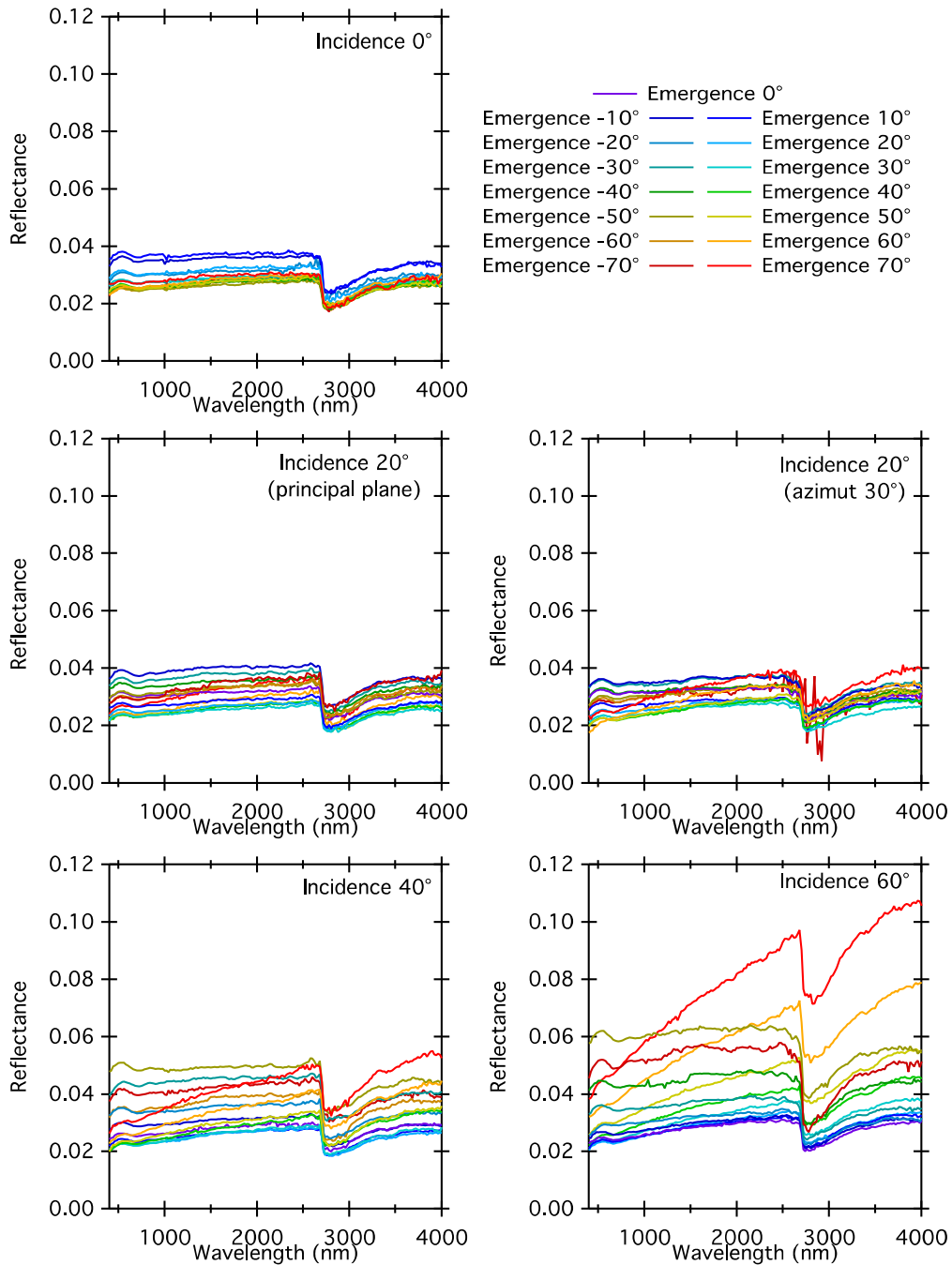
501 The present analysis of the reflectance spectra obtained under NEA-like
 502 temperatures for CM chondrites reveals that, at laboratory timescale, the presence and
 503 so the detection of 700 nm, 900 nm and 3 μ m bands is not affected by temperature,
 504 though the bands can be strongly weakened. Still, a shift of the 700 nm band and a
 505 narrowing of the 3 μ m feature can be predicted for objects that experienced significant
 506 thermal processing. Conversely, the shape and mostly the position of the 700nm and
 507 3 μ m features could potentially be used as a criterion of primitiveness of Ch and Cgh
 508 asteroids.

509

510 **5 Bidirectional reflectance spectroscopy: effects of observation geometry**

511

512 During a flyby or when orbiting around an asteroid, the observation geometry is very
513 variable (incidence, observation and azimuth angles), and differ from the observation
514 geometry under which laboratory data are typically obtained. This geometry depends on
515 the incidence angle of the sunlight on the surface, and the position of the spacecraft.
516 Figure 11 presents the resulting spectra of the powdered Mukundpura meteorite. The
517 same set of spectra was also acquired on the **meteoritic chip**.



518

519 **Figure 11: Complete set of spectra of the powdered Mukundpura meteorite**
 520 **acquired in bidirectional reflectance distribution function mode. Each panel**
 521 **corresponds to an incidence angle: 0° (top panel), 20° in the principal plane**
 522 **(middle left panel) and at 30° azimuth (middle right panel), 40° (bottom left**
 523 **panel) and 60° (bottom right panel).**

524 The dependence of the reflectance spectra to the geometrical configuration is
525 easily seen on Figure 11. Spectra acquired with an incidence angle of 0° present the
526 same slope, and the photometric level stays between 2 and 4% of reflectance, whatever
527 the emergence angle. But spectra acquired under an incidence angle of 60° show drastic
528 variations according to emergence angle. The reflectance value at $4\ \mu\text{m}$ spreads from 2
529 to 11%, and **an increase of the spectral slope is observed with increasing phase**
530 **angle, an effect called phase reddening.**

531

532 In this section, we investigate the different variations of the reflectance spectra
533 when the geometrical configuration is changed. As the two samples, **the chip** and
534 powder have been analyzed under the same set of geometrical configurations, variations
535 due to the texture of the sample can also be analyzed.

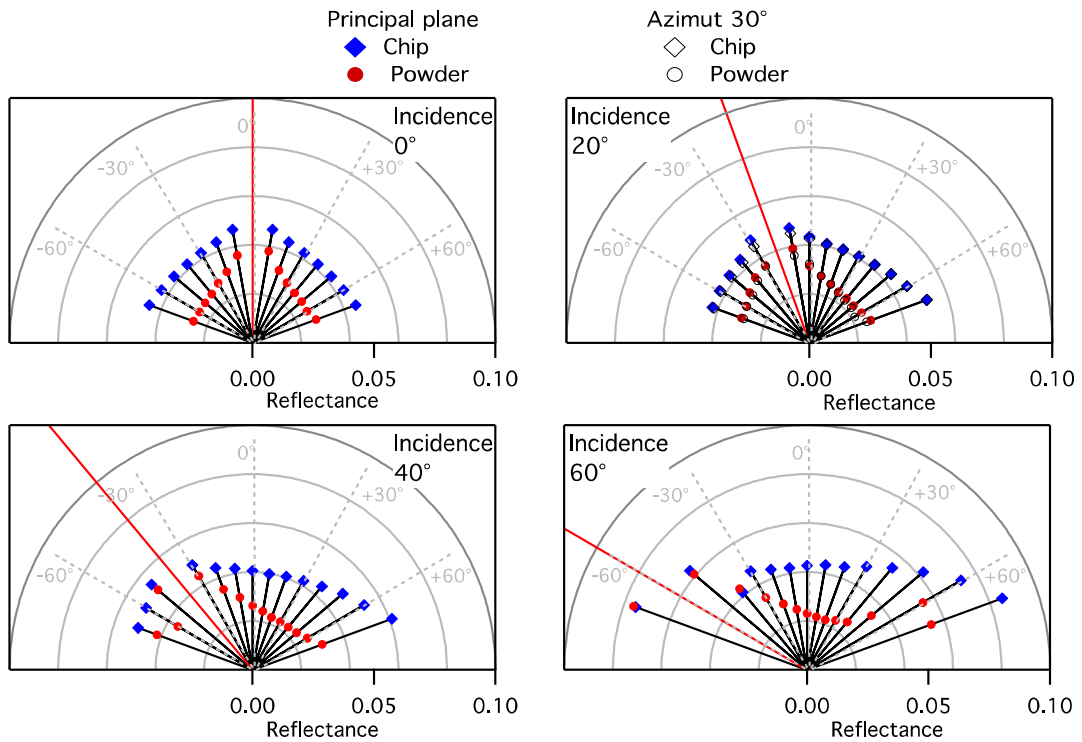
536

537 5.1 Photometric dependence with the geometry

538

539 The bidirectional reflectance distribution function (BRDF) presented on Figure
540 12 displays the measured reflectance values at different emergence angles for several
541 incidence angles. The polar representation of a BRDF enables a quick overview of the
542 distribution of the reflected light (see Figure 12). In this representation, the BRDF of a
543 perfectly lambertian surface would appear as a half circle.

544



545

546 **Figure 12: Bidirectional reflectance distribution function of Mukundpura at**
 547 **560nm. The red line represents the incidence angle and the value of reflectance at**
 548 **each emergence angle is displayed by the colored dots (Blue diamonds: meteoritic**
 549 **chip in the principal plane. Red circles: powder in the principal plane. Open**
 550 **squares: raw meteorite at 30° azimuth angle and 20° incidence angle. Open**
 551 **circles: powder at 30° azimuth angle and 20° incidence angle).**

552 For all geometrical configurations investigated, the **chip** presents a higher
 553 reflectance than the powder. The causes of this effect have been already discussed in 3.2.

554 The BRDFs shows an increase in reflectivity around the incidence direction
 555 (backscattering) and towards high phase angles (forward scattering). It is important to
 556 note that both samples show these two behaviors, being more marked when the
 557 incidence is close to grazing (60°) and more pronounced on the powder.

558 Irregularities in the shape, composition, and refractive index of the particle will
 559 broaden the forward and backward scattering (Hapke 2002).

560

561 This increase of reflectance with decreasing phase angle (backscattering) is due
562 to a combination of two effects. First, the shadows hiding opposition effect (SHOE)
563 where, at phase angle close to 0° , the shadow of one particle over the others around is
564 the smallest, resulting in a strong increase of reflectance in the incidence direction
565 (Hapke 1986). The second process is the coherent backscattering opposition effect
566 (CBOE) describing constructive interferences of the light scattered coherently backward
567 (Hapke 2002). However, this effect only occurs at very low phase angle, not observable
568 in our experiment.

569

570 To make the powder, the original sample was manually powdered but not sieved,
571 leaving a large distribution of grain sizes. The surface texture of the powder can then be
572 seen as rougher than the **chip**. The SHOE effect is weaker in case of the **meteoritic chip**
573 as the sample is compact, with little porosity, limiting shadowing of one particle over
574 another. The variation of the BRDF with grain size has already been investigated
575 (Dozier, Schneider, and McGinnis 1981; Pommerol and Schmitt 2008a; Reddy et al.
576 2015).

577

578 Backward scattering has been observed on several small bodies of the Solar
579 System and is often linked to the study of the surface regolith (Belskaya and Shevchenko
580 2000). Conversely, the study of the bidirectional scattering behavior of a small body,
581 more importantly the strength of the forward scattering and backscattering lobes, can
582 be used to determine the **texture, more importantly the presence of dust** on the
583 surface.

584

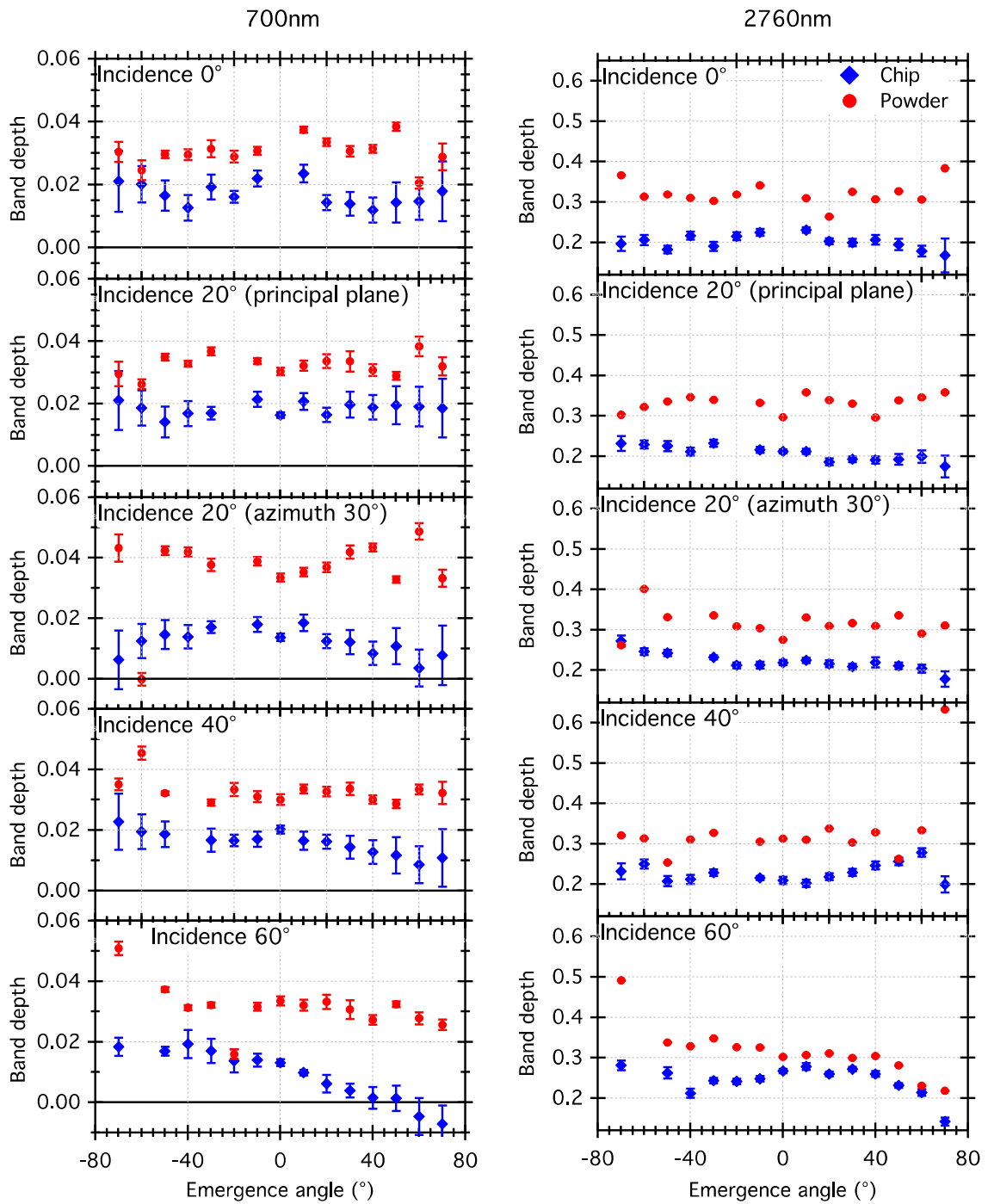
585 5.2 Bidirectional dependence of the absorption features

586

587 The presence of absorption bands in the reflectance spectra of asteroids is, with
588 the spectral slope, commonly used as a criterion to classify small bodies. For example, C-
589 types asteroids exhibits hydration related features around 0.7 μm and 3 μm (Takir and
590 Emery 2012). In this section, we present the influence of observation geometry on the
591 detection and depth of absorption features in the bidirectional reflectance spectra of
592 Mukundpura.

593

594 For both the **chip** and powdered samples, the band depths of the 700 nm and 2760
595 nm features are calculated according to the formula in section 3.2. The results are
596 presented in Figure 13.



597

598 **Figure 13: Band depth of the 700nm (left) and the 2760nm (left) absorption**
 599 **features of Mukundpura for the different geometries. Note the different vertical**
 600 **scales.**

601

602 First, it is important to note that the absorption features detected on the

603 **meteoritic chip** are generally fainter than for the powdered sample's spectra, in all
604 observation geometries studied. Previous laboratory measurements have shown
605 variation in the band depth of absorption features as a function of geometrical
606 configurations, mostly the decrease of band depth at larger phase angles (Pommerol and
607 Schmitt 2008a; Beck et al. 2012, 2011). This effect is generally explained by an increase
608 of the relative number of photons scattered out of the sample before entering any of the
609 grains. Radiative transfer modeling confirms this hypothesis (Pommerol and Schmitt
610 2008a).

611

612 But several behaviors are observed with our measurements, **depending on** the
613 incidence angle, not only the phase angle. **For illuminations near nadir**, the band
614 depth decreases until phase angle around 40° , then increases with the phase angle. **In**
615 **case of grazing illumination, the band depth only decreases with increasing phase**
616 **angle.**

617

618 In case of the iron 700nm feature at grazing incidence (60°), the band disappears
619 from the spectra at phase angles larger than 90° , but only on the raw sample. For the
620 powder, the iron band is detectable at all geometrical configurations and the general
621 trend leads us to think that the band will be detectable even at phase angle larger than
622 120° . The hydration feature at 2760nm is detectable through all our measurements, but
623 begins to fade at 110° phase angle until reaching a depth of 14% at 130° , the largest
624 phase angle studied. According to this trend, the band will also disappear from the
625 spectra, at phase angles greater than 140° or 150° but these are clearly extreme
626 conditions of observation.

627

628 The geometry of illumination and observation has an important impact in the
629 depth of the absorption bands. Under all observation geometries, the band depths are
630 stronger for the powder than for the **chip**. The depth of the 3 μ m band is variable with
631 the observation geometry but it is always significant. The depth of the 0.7 μ m band is
632 also variable with observation geometry but can disappear under extreme geometries.
633 Nevertheless, for ground-based observations, mostly obtained at low phase angle, the
634 observation geometry cannot explain the disappearance of the 0.7 μ m band.

635

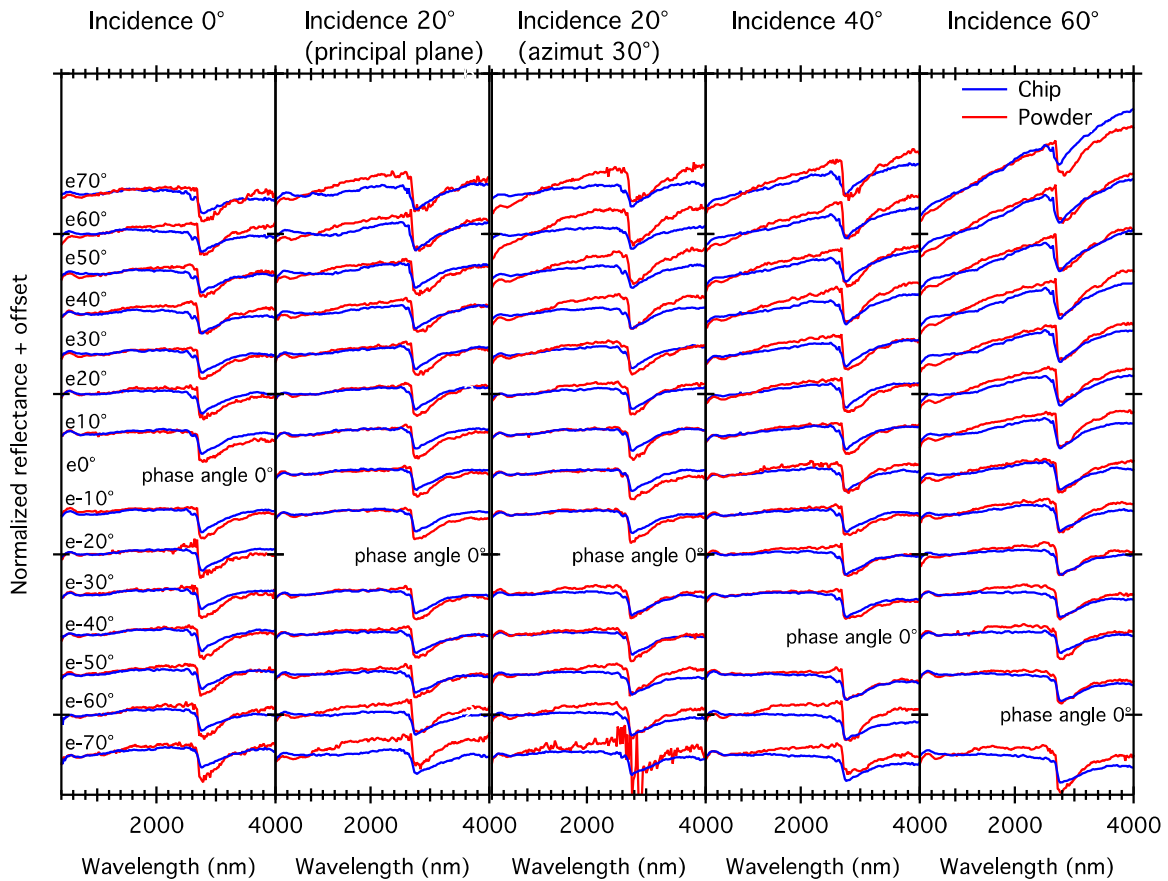
636

637 5.3 Geometry dependency of the spectral slope

638 5.3.1 Phase reddening

639

640 Reflectance spectra of most carbonaceous chondrites present a faint red slope,
641 even if blue-sloped spectra can occur under specific conditions (Cloutis et al. 2013). **The**
642 **phase reddening observed on the reflectance spectra of Mukundpura (Figure 11)**
643 results from the wavelength dependence of the single-scattering albedo (Gradie and
644 Veverka 1986). This phenomenon was observed on asteroids such as (4) Vesta (Gehrels
645 et al. 1970; Blanco and Catalano 1979), on several Main Belt asteroids (Beth E. Clark et
646 al. 2002), NEAs (Sanchez et al. 2012) and on the Moon (Lane and Irvine 1973; Johnson et
647 al. 2013) and more recently on (101955) Bennu (Binzel et al. 2015). On our spectra, this
648 effect is more important at high incidence angle (at 60°), where observations have been
649 made at the largest phase angles. To have a better overview of the spectral reddening
650 and its dependency with observation geometry Figure 14 presents all spectra after
651 normalization to unity at 1000 nm.



652

653 **Figure 14: Reflectance spectra of the Mukundpura meteorite normalized at**
 654 **1000nm (Blue: chip, Red: powder) taken under different geometrical**
 655 **configurations. Offset for clarity.**

656

657

658

659

660

661

662

663

664

Sanchez et al. (2012) determined the spectral slope as the fitted linear continuum between 0.7 and 1.55 μm . This method is commonly used around absorption bands or for measurements on a limited spectral range, but in case of wider spectral ranges, the continuum should not be considered as linear (Parente et al. 2011). The spectral slope can also be calculated as the ratio between the reflectance measured at two separated wavelength, in the visible (Schröder et al. 2014), or between the maximum of reflectance value and the absolute reflectance at 1.5 μm (Cloutis et al. 2011) In our case, the spectral range is too wide to adopt a linear approach to the continuum, thus we the spectral slope as a color ratio.

665

666 The value of the spectral slope is calculated as the ratio between the reflectance

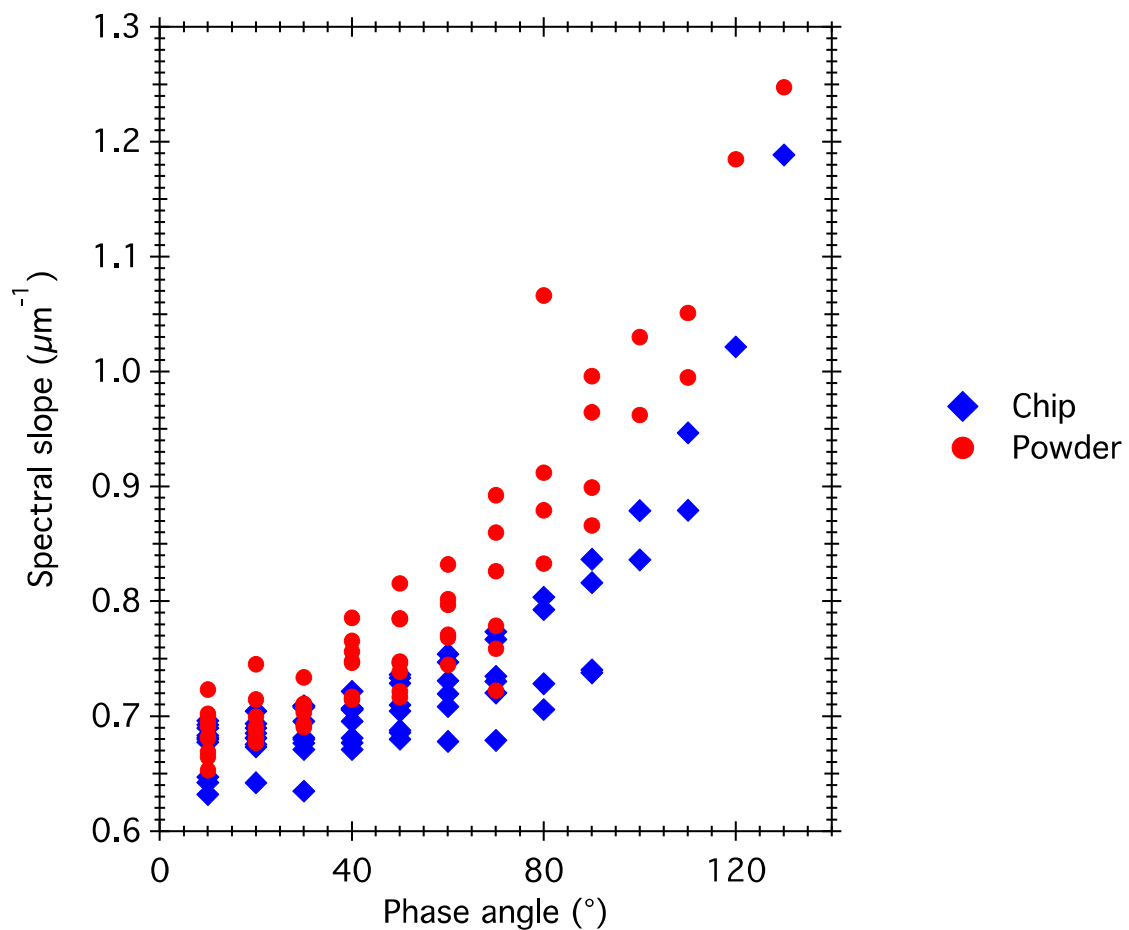
667 at 2000 nm and the reflectance at 500 nm:

669
$$\text{Spectral slope } (\mu\text{m}^{-1}) = \frac{1}{1.5} \frac{\text{Reflec}_{2000 \text{ nm}}}{\text{Reflec}_{500 \text{ nm}}}$$

668

670 The variation of the spectral slope with phase angle is displayed on Figure 15, for

671 both sets of spectra.



672

673 **Figure 15: Effect of the phase angle on the spectral slope of the reflectance spectra**
674 **(spectral reddening) of the raw Mukundpura meteorite and its powder.**

675

676 The reflectance spectra of the powder are redder-sloped than the spectra of the

677 raw meteorite. At low phase angle, the raw meteorite spectra have a slope of
678 0.6721 ± 0.023 while the powder displays a slope of 0.6861 ± 0.021 . This value is averaged
679 over the 10 configurations with a phase angle of 10° and the error corresponds to the
680 standard deviation. At the largest phase angle studied, $g = 130^\circ$, the slope of the **chip**
681 spectrum reaches 1.1885 ± 0.0064 compared to 1.2474 ± 0.0090 for the powder spectrum.

682

683 Previous investigations pointed out that the surface particle density and texture
684 can radically change the spectral slope from slightly blue to strongly red (Binzel et al.
685 2015; Britt and Pieters 1988). **Cloutis, Hiroi, et al. (2011)** showed that a change of
686 porosity applied to the same sample can induce a change in the spectral slope. But the
687 abundance of opaque minerals in the chondrite should not induce significant effects on
688 the spectral reddening (**Cloutis, Hudon, et al. 2011**). Several laboratory measurements
689 showed that larger grains also induce less red-sloped reflectance spectra (**Binzel et al.**
690 **2015; Gillis-Davis et al. 2013; Johnson and Fanale 1973; Cloutis, Hudon, et al.**
691 **2011; Cloutis et al. 2013**).

692

693 The variation of slope with the phase angle, i.e. the phase reddening, is
694 pronounced for both raw meteorite and powder. We found that the spectral slope does
695 not vary linearly with the phase angle and that the curve of spectral reddening is
696 different between the meteorite and the powder. In our case, the spectral reddening of
697 the powder is more pronounced at low phase angle but both samples reach roughly the
698 same value at high phase angles. The difference in porosity and granulometry between
699 the two samples induces changes in the spectral slopes. **Recently, the analysis of phase**
700 **reddening has been used to highlight the presence of regolith at the surface of the**
701 **large boulders of Bennu (DellaGiustina et al. 2019).**

702

703

5.3.2 Bidirectional dependency of the spectral slope

704

705

706

707

708

709

710

711

712

713

714

715

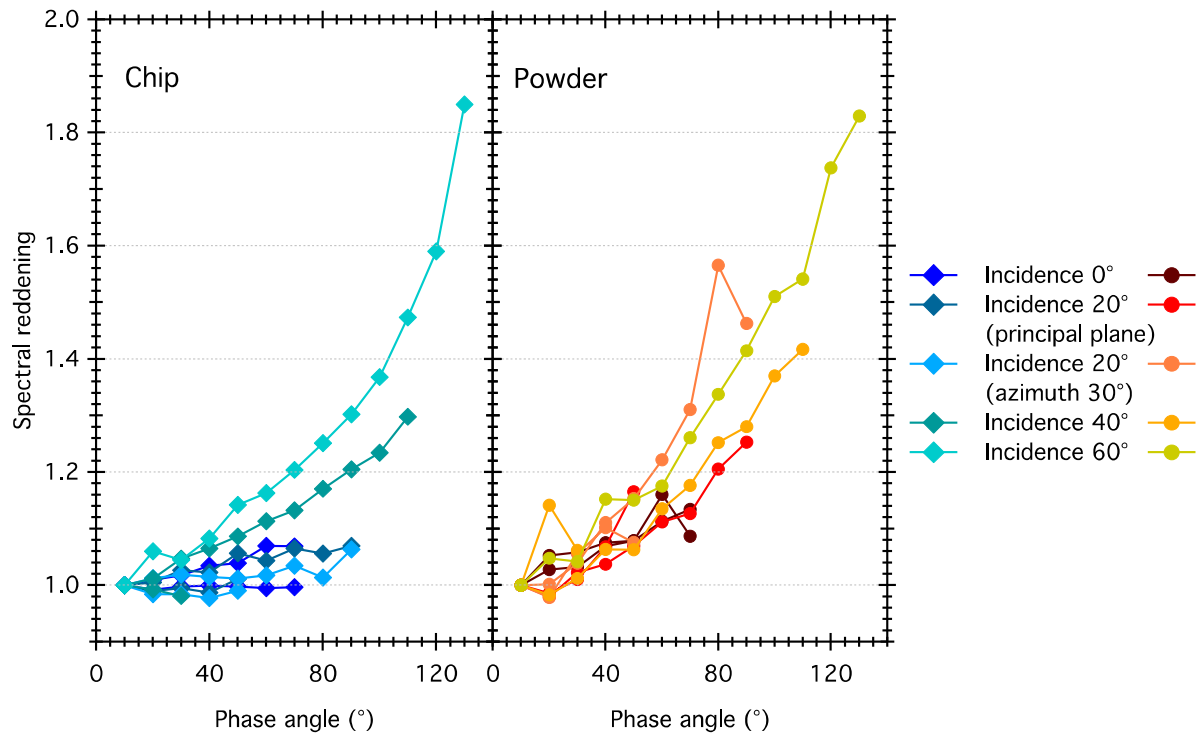
716

The value of the spectral slope varies with increasing phase angle, as it has been measured for example by the Hayabusa spacecraft on the NEA Itokawa (Abe et al. 2006). Reflectance spectra of the asteroid acquired with a phase angle of 30° showed a spectral slope 6% redder than the spectra at 8° (Abe et al. 2006). This effect was also measured on the NEA (433) Eros, with an increase of the spectral slope reaching 11% between phase angles of 0° and 100° (Clark et al. 2002).

The spectral reddening is calculated for each sample as the ratio between the spectral slope at a given phase angle and the spectral slope at the lowest phase angle g available, so 10°.

$$\text{Spectral Reddening} = \frac{\text{Spectral slope } g}{\text{Spectral slope }_{g=10^\circ}}$$

For the two types of surfaces and for each incidence angle, the spectral reddening of the spectra is displayed in Figure 16.



717

718 **Figure 16: Spectral reddening of the reflectance spectra of the chip (left) and**
 719 **ground (right) Mukundpura meteorite for each incidence angle.**

720

721 Both samples show a dependence of the reddening, not only with phase angle but
 722 also with incidence angle. For a phase angle of 70°, the reddening reaches 1.07 ± 0.01 for
 723 the **meteoritic chip** and 1.13 ± 0.02 for the powder measured at nadir incidence, while it
 724 reaches 1.20 ± 0.01 for the **chip** and 1.26 ± 0.01 for the powder for the same phase angle
 725 but at incidence 60°. At low incidence angle ($\leq 20^\circ$) the spectral reddening of the **chip**
 726 always remains weak (< 1.07) even at phase angle as high as 90°, while for the powder
 727 the reddening increases steadily even at nadir illumination and is already larger than 1.2
 728 at 80° phase angle. Conversely the spectral reddening seems to depend on the incidence
 729 angle at all phase angles for the **chip**, while for the powder the effect is noticeable only
 730 above 60°. Our observations reveal that spectral reddening could be used to detect the

731 presence, or absence of a **fine-grained** regolith on the surface of a small body by looking
732 at phase reddening at low incidence angle.

733

734 Neither the spectral slope nor the spectral reddening show a linear relation with
735 the phase angle, but rather an exponential dependence. MBAs can only be observed with
736 ground-based telescopes at phase angles smaller than 30° , where the reddening is
737 modest (between 1.01 and 1.06 for the powder sample and between 0.98 and 1.05 for
738 the raw meteorite). However, NEAs can be observed over a wider range of phase angles,
739 from opposition to 90° (Sanchez et al. 2012). In this configuration, the reddening of the
740 spectra can reach 1.46 for a **dust-covered surface** and 1.3 in case of a raw surface.

741

742 Particular attention to phase reddening should be given as the variation of
743 spectral slope in asteroid observations is generally mainly attributed to space
744 weathering (irradiation by cosmic ions and micro-meteorites bombardment) (Hapke
745 2001; Chapman 2004; Clark et al. 2002). Several laboratory studies irradiated meteoritic
746 samples, either with ions or pulsed laser radiations, in order to reproduce the processes
747 occurring on airless bodies. Using the meteorite Epinal, (Strazzulla et al. 2005) showed
748 that ion irradiation increases the spectral slope by a factor of 6 and, comparing the
749 experimental results with spectra of several NEAs, evaluated the timescale for
750 weathering the near-earth asteroids between 10^4 and 10^6 years. (Sanchez et al. 2012)
751 measured reflectance spectra on three ordinary chondrites and found that an increase of
752 30° to 120° of phase angle can mimic the reddening of the reflectance spectrum induced
753 by 0.1×10^6 to 1.3×10^6 years of irradiation at 1AU from the Sun. So in case of NEAs, the
754 geometry of observation can induce the same reddening of the spectra as space
755 weathering.

756

757 6 CONCLUSION

758 Laboratory reflectance spectroscopy can help understand the specificities of C-
759 complex NEAs observations when compared to C-type MBAs. We have shown that
760 temperature, surface texture, as well as observation geometry (incidence, emergence
761 and azimuth angle) can all have an impact on reflectance spectra. When comparing
762 **chips** and powdered samples, we found that:

763 -Both samples display spectral signatures of hydration and thus the absence, or
764 presence, of a **fine-grained** regolith at the surface cannot explain the lack of hydrated
765 NEAs.

766 - **Dust** covered surfaces are expected to be darker than rock covered surfaces
767 because of the apparent homogeneity of the composition of the powder compared to the
768 heterogeneity of the surface of the raw meteorite clearly displaying clasts and inclusions
769 inside a dark matrix.

770 -BRDF analysis of the two samples shows that the **powdered sample** presents
771 stronger forward scattering and backscattering lobes compared to the raw meteorite.
772 This is due to the SHOE, increased by the rougher texture of the powder.

773 -Absorption features appear fainter in the case of the raw sample, due to the
774 higher amount of photons being scattered out of the surface before having entered the
775 sample. Following this result, absorption features should be more difficult to detect on
776 surfaces lacking **fine-grained** regolith, i.e. rubble pile NEAs.

777 -At large phase angle, the reflectance spectra of the **powdered sample** present a
778 steeper spectral slope compared to the measurement on the **chip**.

779 -Spectral reddening of the powder appears relatively insensitive to the incident
780 angle while for the raw meteorite at a given phase angle, the reflectance spectra are
781 redder when the illumination approaches grazing incidence.

782

783 The surface temperature experienced by NEAs can have an effect on their
784 spectral signatures. The temperature affects the reflectance spectra of a meteorite,
785 mostly by modifying the depth, position and width of the iron features around 700nm
786 and 900nm. Our measurements show that at laboratory timescale, irreversible
787 alterations of the sample can be induced by only one heating-cooling cycle, simulating
788 successively the sunrise and sunset on the surface of the small body. The hydration
789 feature at 3 μ m becomes fainter but is still detectable on the reflectance spectra.
790 However, our series of measurements after a single thermal cycle at high temperature
791 do not allow us to make any assumption on the possible disappearance of the features
792 after numerous cycles of heating and cooling. Further investigations of these irreversible
793 alterations are currently conducted.

794 Several effects due to the geometrical configuration of observation have been
795 highlighted by our measurements. First, carbonaceous chondrites do not behave as a
796 lambertian surface in the VNIR. Second the spectral slope and the depths of the
797 absorption features are impacted by the direction of illumination and the emergence
798 angle. Most importantly, our results show that in the case of the raw meteorite the
799 hydration signatures in the visible range disappear from the reflectance spectra at large
800 phase angle. Keeping in mind that NEAs can be observed at larger phase angles
801 compared to MBAs, and that their surfaces seem depleted in **fine-grained** regolith, this
802 geometry effect could also contribute to the apparent dehydration of NEAs.

803

804 **Acknowledgments**

805 Sandra Potin is supported by Université Grenoble Alpes (UGA) (IRS IDEX/UGA). Pierre
806 Beck acknowledges funding from the H2020 European Research Council (ERC)
807 (SOLARYS ERC-CoG2017_771691). The instrument SHADOWS is funded by the Agence
808 Nationale de la Recherche (ANR) (Labex OSUG@2020, ANR10 LABX56), the Horizon
809 2020 Framework Programme (H2020) (654208) and the Centre National d'Études
810 Spatiales (CNES).

811

812 **References**

813 Abe, M., Y. Takagi, K. Kitazato, S. Abe, T. Hiroi, F. Vilas, B. E. Clark, et al. 2006. "Near-
814 Infrared Spectral Results of Asteroid Itokawa from the Hayabusa Spacecraft."
815 *Science* 312 (5778): 1334–38. <https://doi.org/10.1126/science.1125718>.

816 Beck, P., J. A. Barrat, F. Grisolles, E. Quirico, B. Schmitt, F. Moynier, P. Gillet, and C. Beck.
817 2011. "NIR Spectral Trends of HED Meteorites: Can We Discriminate between the
818 Magmatic Evolution, Mechanical Mixing and Observation Geometry Effects?" *Icarus*
819 216 (2): 560–71. <https://doi.org/10.1016/j.icarus.2011.09.015>.

820 Beck, P., A. Pommerol, N. Thomas, B. Schmitt, F. Moynier, and J. A. Barrat. 2012.
821 "Photometry of Meteorites." *Icarus* 218 (1): 364–77.
822 <https://doi.org/10.1016/j.icarus.2011.12.005>.

823 Beck, P., B. Schmitt, E. A. Cloutis, and P. Vernazza. 2015. "Low-Temperature Reflectance
824 Spectra of Brucite and the Primitive Surface of 1-Ceres?" *Icarus* 257 (June): 471–76.

825 <https://doi.org/10.1016/j.icarus.2015.05.031>.

826 Beck, P, E Quirico, G Montes-hernandez, L Bonal, J Bollard, F Orthous-daunay, K T
827 Howard, et al. 2010. "Hydrous Mineralogy of CM and CI Chondrites from Infrared
828 Spectroscopy and Their Relationship with Low Albedo Asteroids." *Geochimica et*
829 *Cosmochimica Acta* 74 (16): 4881–92. <https://doi.org/10.1016/j.gca.2010.05.020>.

830 Belskaya, I. N., and V. G. Shevchenko. 2000. "Opposition Effect of Asteroids." *Icarus* 147
831 (1): 94–105. <https://doi.org/10.1006/icar.2000.6410>.

832 Benner, Lance A.M., Steven J. Ostro, Christopher Magri, Michael C. Nolan, Ellen S. Howell,
833 Jon D. Giorgini, Raymond F. Jurgens, et al. 2008. "Near-Earth Asteroid Surface
834 Roughness Depends on Compositional Class." *Icarus* 198 (2): 294–304.
835 <https://doi.org/10.1016/j.icarus.2008.06.010>.

836 Binzel, Richard P., Francesca E. DeMeo, Brian J. Burt, Edward A. Cloutis, Ben Rozitis,
837 Thomas H. Burbine, Humberto Campins, et al. 2015. "Spectral Slope Variations for
838 OSIRIS-REx Target Asteroid (101955) Bennu: Possible Evidence for a Fine-Grained
839 Regolith Equatorial Ridge." *Icarus* 256: 22–29.
840 <https://doi.org/10.1016/j.icarus.2015.04.011>.

841 Blanco, C, and S Catalano. 1979. "UBV Photometry of Vesta." *Icarus* 40: 350–63.
842 [https://doi.org/https://doi.org/10.1016/0019-1035\(79\)90028-9](https://doi.org/https://doi.org/10.1016/0019-1035(79)90028-9).

843 Bland, P. A., G. S. Collins, T. M. Davison, N. M. Abreu, F. J. Ciesla, A. R. Muxworthy, and J.
844 Moore. 2014. "Pressure-Temperature Evolution of Primordial Solar System Solids

845 during Impact-Induced Compaction." *Nature Communications* 5: 1–13.
846 <https://doi.org/10.1038/ncomms6451>.

847 Brearley, Adrian J. 2006. "The Action of Water." In *Meteorites and the Early Solar System*
848 *II*, 587–624. <https://doi.org/10.1039/AN9214600270>.

849 Brissaud, Olivier, Bernard Schmitt, Nicolas Bonnefoy, Sylvain Douté, Patrick Rabou, Will
850 Grundy, and Michel Fily. 2004. "Spectrogonio Radiometer for the Study of the
851 Bidirectional Reflectance and Polarization Functions of Planetary Surfaces. 1.
852 Design and Tests." *Applied Optics* 43 (9): 1926–37.
853 <https://doi.org/10.1364/AO.43.001926>.

854 Britt, D. T., and C. M. Pieters. 1988. "Bidirectional Reflectance Properties of Iron-Nickel
855 Meteorites." In *18th LPSC*, 503–12.

856 Burns, R.G. 1993. *Mineralogical Applications of Crystal Field Theory, Second Edition*.
857 Cambridge University Press.

858 Carry, B., E. Solano, S. Eggl, and F. E. DeMeo. 2016. "Spectral Properties of Near-Earth
859 and Mars-Crossing Asteroids Using Sloan Photometry." *Icarus* 268: 340–54.
860 <https://doi.org/10.1016/j.icarus.2015.12.047>.

861 Chapman, Clark R. 2004. "Space Weathering of Asteroid Surfaces." *Annual Review of*
862 *Earth and Planetary Sciences* 32 (1): 539–67.
863 <https://doi.org/10.1146/annurev.earth.32.101802.120453>.

864 Clark, Beth E., P. Helfenstein, J. F. Bell, C. Peterson, J. Veverka, N. I. Izenberg, D.
865 Domingue, D. Wellnitz, and Lucy McFadden. 2002. "NEAR Infrared Spectrometer
866 Photometry of Asteroid 433 Eros." *Icarus* 155 (1): 189–204.
867 <https://doi.org/10.1006/icar.2001.6748>.

868 Clark, Beth Ellen, Bruce Hapke, Carle Pieters, and Daniel Britt. 2002. "Asteroid Space
869 Weathering and Regolith Evolution." In *Asteroids III*, 585–99.
870 [https://doi.org/10.1016/0273-1177\(91\)90551-T](https://doi.org/10.1016/0273-1177(91)90551-T).

871 Cloutis, E. A., T. Hiroi, M. J. Gaffey, C. M.O.D. Alexander, and P. Mann. 2011. "Spectral
872 Reflectance Properties of Carbonaceous Chondrites: 1. CI Chondrites." *Icarus* 212
873 (1): 180–209. <https://doi.org/10.1016/j.icarus.2010.12.009>.

874 Cloutis, E. A., P. Hudon, T. Hiroi, M. J. Gaffey, and P. Mann. 2011. "Spectral Reflectance
875 Properties of Carbonaceous Chondrites: 2. CM Chondrites." *Icarus* 216 (1): 309–46.
876 <https://doi.org/10.1016/j.icarus.2011.09.009>.

877 Cloutis, Edward A., P. Hudon, Takahiro Hiroi, Michael J. Gaffey, Paul Mann, Conel M. O'D.
878 Alexander, James F. Bell III, and Beth Ellen Clark. 2013. "Possible Causes of Blue
879 Slopes (~0.5-2.5 Mm) in Carbonaceous Chondrite Spectra." *44th Lunar and*
880 *Planetary Science Conference*, 1550.

881 Cloutis, Edward A., Kaitlyn A. McCormack, James F. Bell, Amanda R. Hendrix, Daniel T.
882 Bailey, Michael A. Craig, Stanley A. Mertzman, Mark S. Robinson, and Miriam A.
883 Riner. 2008. "Ultraviolet Spectral Reflectance Properties of Common Planetary
884 Minerals." *Icarus* 197 (1): 321–47. <https://doi.org/10.1016/j.icarus.2008.04.018>.

- 885 Cloutis, Edward A., Valerie B. Pietrasz, Cain Kiddell, Matthew R.M. Izawa, Pierre
886 Vernazza, Thomas H. Burbine, Francesca DeMeo, et al. 2018. "Spectral Reflectance
887 'Deconstruction' of the Murchison CM2 Carbonaceous Chondrite and Implications
888 for Spectroscopic Investigations of Dark Asteroids." *Icarus* 305: 203–24.
889 <https://doi.org/10.1016/j.icarus.2018.01.015>.
- 890 Delbo, Marco, and Patrick Michel. 2011. "Temperature History and Dynamical Evolution
891 of (101955) 1999 RQ 36: A Potential Target for Sample Return from a Primitive
892 Asteroid." *Astrophysical Journal Letters* 728 (2 PART II): 1–5.
893 <https://doi.org/10.1088/2041-8205/728/2/L42>.
- 894 DellaGiustina, D. N., J. P. Emery, D. R. Golish, B. Rozitis, C. A. Bennett, K. N. Burke, R. L.
895 Ballouz, et al. 2019. "Properties of Rubble-Pile Asteroid (101955) Bennu from
896 OSIRIS-REx Imaging and Thermal Analysis." *Nature Astronomy* 3 (4): 341–51.
897 <https://doi.org/10.1038/s41550-019-0731-1>.
- 898 Dozier, Jeff, Stanley R. Schneider, and David F. McGinnis. 1981. "Effect of Grain Size and
899 Snowpack Water Equivalence on Visible and Near-infrared Satellite Observations of
900 Snow." *Water Resources Research* 17 (4): 1213–21.
901 <https://doi.org/10.1029/WR017i004p01213>.
- 902 Dunn, Tasha L., Thomas H. Burbine, William F. Bottke, and John P. Clark. 2013.
903 "Mineralogies and Source Regions of Near-Earth Asteroids." *Icarus* 222 (1): 273–82.
904 <https://doi.org/10.1016/j.icarus.2012.11.007>.
- 905 Fornasier, S., C. Lantz, M. A. Barucci, and M. Lazzarin. 2014. "Aqueous Alteration on Main

906 Belt Primitive Asteroids: Results from Visible Spectroscopy." *Icarus* 233: 163–78.
907 <https://doi.org/10.1016/j.icarus.2014.01.040>.

908 Fujiwara, A, J Kawaguchi, D K Yeomans, M Abe, T Mukai, T Okada, J Saito, et al. 2006.
909 "The Rubble-Pile Asteroid Itokawa as Observed by Hayabusa." *Science* 312 (5778):
910 1330–34. <https://doi.org/10.1126/science.1125841>.

911 Garenne, A., P. Beck, G. Montes-Hernandez, R. Chiriac, F. Toche, E. Quirico, L. Bonal, and
912 B. Schmitt. 2014. "The Abundance and Stability of 'Water' in Type 1 and 2
913 Carbonaceous Chondrites (CI, CM and CR)." *Geochimica et Cosmochimica Acta* 137:
914 93–112. <https://doi.org/10.1016/j.gca.2014.03.034>.

915 Gehrels, T, E Roemer, R.C. Taylor, and B.H Zllner. 1970. "Minor Planets and Related
916 Objects. IV. Asteroid (1566) Icarus." *The Astronomical Journal* 75 (2): 186–95.

917 Ghosh, Weidenschilling, McSween, and Rubin. 2006. "Asteroidal Heating and Thermal
918 Stratification of the Asteroid Belt." In *Meteorites and the Early Solar System II*, 555–
919 66. <https://doi.org/10.1152/ajpgi.00524.2002>.

920 Gillis-Davis, Jeffrey J., P.G. Lucey, J. P. Bradley, H. Ishii, and H. C. Connolly. 2013. "LASER
921 SPACE WEATHERING OF ALLENDE METEORITE." *44th Lunar and Planetary Science
922 Conference*, 2494. <https://doi.org/10.1029/2005JE002544>.

923 Gradie, J, and J. Veverka. 1986. "The Wavelength Dependence of Phase Coefficients."
924 *Icarus* 66: 455–67.

- 925 Grimm, R.E., and H.Y. Mcswen. 1993. "Heliocentric Zoning of the Asteroid Belt by
926 Aluminum-26." *Science* 259: 653–55.
- 927 Grimm, Robert E., and Harry Y. Mcswen. 1989. "Water and the Thermal Evolution of
928 Carbonaceous Chondrite Parent Bodies." *Icarus* 82 (2): 244–80.
929 [https://doi.org/10.1016/0019-1035\(89\)90038-9](https://doi.org/10.1016/0019-1035(89)90038-9).
- 930 Grisolle, F, B Schmitt, P Beck, S Philippe, and O Brissaud. 2014. "Experimental Simulation
931 of the Condensation and Metamorphism of Seasonal CO2 Condensates under
932 Martian Conditions." In *EPSC Abstracts*, 9:EPSC2014-635.
- 933 Hamilton, V. E., A A Simon, P R Christensen, D. Reuter, B. E. Clark, M A Barucci, N.E.
934 Bowles, et al. 2019. "Evidence for Widespread Hydrated Minerals on Asteroid
935 (101955) Bennu." *Nature Astronomy* 3 (101955): 332–40.
936 <https://doi.org/https://doi.org/10.1038/s41550-019-0722-2>.
- 937 Hapke, Bruce. 1981. "Bidirectional Reflectance Spectroscopy: 1. Theory." *Journal of*
938 *Geophysical Research: Solid Earth* 86 (B4): 3039–54.
939 <https://doi.org/10.1029/JB086iB04p03039>.
- 940 ———. 1986. "Bidirectional Reflectance Spectroscopy. 4. The Extinction Coefficient and
941 the Opposition Effect." *Icarus* 67 (2): 264–80. [https://doi.org/10.1016/0019-](https://doi.org/10.1016/0019-1035(86)90108-9)
942 [1035\(86\)90108-9](https://doi.org/10.1016/0019-1035(86)90108-9).
- 943 ———. 2001. "Space Weathering from Mercury to the Asteroid Belt." *Journal of*
944 *Geophysical Research* 106: 10039–73. <https://doi.org/doi:10.1029/2000JE001338>.

- 945 ———. 2002. "Bidirectional Reflectance Spectroscopy. 5. The Coherent Backscatter
946 Opposition Effect and Anisotropic Scattering." *Icarus* 157 (2): 523–34.
947 <https://doi.org/10.1006/icar.2002.6853>.
- 948 ———. 2008. "Bidirectional Reflectance Spectroscopy. 6. Effects of Porosity." *Icarus* 195
949 (2): 918–26. <https://doi.org/10.1016/j.icarus.2008.01.003>.
- 950 Hasegawa, Sunao, Thomas G. Müller, Kyoko Kawakami, Toshihiro Kasuga, Takehiko
951 Wada, Yoshifusa Ita, Naruhisa Takato, Hiroshi Terada, Takuya Fujiyoshi, and
952 Masanao Abe. 2008. "Albedo, Size, and Surface Characteristics of Hayabusa-2
953 Sample-Return Target 162173 1999 JU3 from AKARI and Subaru Observations."
954 *Publications of the Astronomical Society of Japan* 60 (SP2): 399–405.
955 <https://doi.org/>.
- 956 Hinrichs, John L., and Paul G. Lucey. 2002. "Temperature-Dependent near-Infrared
957 Spectral Properties of Minerals, Meteorites, and Lunar Soil." *Icarus* 155 (1): 169–80.
958 <https://doi.org/10.1006/icar.2001.6754>.
- 959 Johnson, Jeffrey R., Michael K. Shepard, William M. Grundy, David A. Paige, and Emily J.
960 Foote. 2013. "Spectrogoniometry and Modeling of Martian and Lunar Analog
961 Samples and Apollo Soils." *Icarus* 223 (1): 383–406.
962 <https://doi.org/10.1016/j.icarus.2012.12.004>.
- 963 Johnson, Torrence V, and Fraser P Fanale. 1973. "Optical Properties of Carbonaceous
964 Chondrites and Their Relationship to Asteroids." *Journal of Geophysical Research* 78
965 (35): 8507–18. <https://doi.org/10.1029/JB078i035p08507>.

- 966 Kitazato, K., R. E. Milliken, T. Iwata, M. Abe, M. Ohtake, S. Matsuura, T. Arai, et al. 2019.
967 “The Surface Composition of Asteroid 162173 Ryugu from Hayabusa2 Near-
968 Infrared Spectroscopy.” *Science*, 10.1126/science.aav7432.
969 <https://doi.org/10.1126/science.aav7432>.
- 970 Lane, Adair P, and William M Irvine. 1973. “Monochromatic Phase Curves and Albedos
971 for the Lunar Disk.” *The Astronomical Journal* 78 (3): 267–77.
- 972 Mahan, Brandon, Frédéric Moynier, Pierre Beck, Emily A. Pringle, and Julien Siebert.
973 2018. “A History of Violence: Insights into Post-Accretionary Heating in
974 Carbonaceous Chondrites from Volatile Element Abundances, Zn Isotopes and
975 Water Contents.” *Geochimica et Cosmochimica Acta* 220: 19–35.
976 <https://doi.org/10.1016/j.gca.2017.09.027>.
- 977 Marchi, S., M. Delbo’, A. Morbidelli, P. Paolicchi, and M. Lazzarin. 2009. “Heating of Near-
978 Earth Objects and Meteoroids Due to Close Approaches to the Sun.” *Monthly Notices
979 of the Royal Astronomical Society* 400 (1): 147–53. [https://doi.org/10.1111/j.1365-
980 2966.2009.15459.x](https://doi.org/10.1111/j.1365-2966.2009.15459.x).
- 981 Michel, Patrick, Willy Benz, and Derek C. Richardson. 2003. “Disruption of Fragmented
982 Parent Bodies as the Origin of Asteroid Families.” *Nature* 421 (6923): 608–11.
983 <https://doi.org/10.1038/nature01364>.
- 984 ———. 2004. “Catastrophic Disruption of Asteroids and Family Formation: A Review of
985 Numerical Simulations Including Both Fragmentation and Gravitational
986 Reaccumulations.” *Planetary and Space Science* 52 (12): 1109–17.

- 987 <https://doi.org/10.1016/j.pss.2004.07.008>.
- 988 Nakamura, T. 2005. "Post-Hydration Thermal Metamorphism of Carbonaceous
989 Chondrites." *Journal of Mineralogical and Petrological Sciences* 100: 260–72.
- 990 Nakamura, Tomoki. 2006. "Yamato 793321 CM Chondrite: Dehydrated Regolith Material
991 of a Hydrous Asteroid." *Earth and Planetary Science Letters* 242 (1–2): 26–38.
992 <https://doi.org/10.1016/j.epsl.2005.11.040>.
- 993 Parente, Mario, Heather D. Makarewicz, and Janice L. Bishop. 2011. "Decomposition of
994 Mineral Absorption Bands Using Nonlinear Least Squares Curve Fitting: Application
995 to Martian Meteorites and CRISM Data." *Planetary and Space Science* 59 (5–6): 423–
996 42. <https://doi.org/10.1016/j.pss.2011.01.009>.
- 997 Pommerol, Antoine, and Bernard Schmitt. 2008a. "Strength of the H₂O Near-Infrared
998 Absorption Bands in Hydrated Minerals: Effects of Measurement Geometry." *Journal*
999 *of Geophysical Research E: Planets* 113 (12): E12008.
1000 <https://doi.org/10.1029/2008JE003197>.
- 1001 ———. 2008b. "Strength of the H₂O Near-Infrared Absorption Bands in Hydrated
1002 Minerals: Effects of Particle Size and Correlation with Albedo." *Journal of*
1003 *Geophysical Research* 113 (E10): E10009. <https://doi.org/10.1029/2007JE003069>.
- 1004 Pommerol, Antoine, Bernard Schmitt, Pierre Beck, and Olivier Brissaud. 2009. "Water
1005 Sorption on Martian Regolith Analogs: Thermodynamics and near-Infrared
1006 Reflectance Spectroscopy." *Icarus* 204 (1): 114–36.

- 1007 <https://doi.org/10.1016/j.icarus.2009.06.013>.
- 1008 Potin, Sandra, Olivier Brissaud, Pierre Beck, Bernard Schmitt, Yves Magnard, Jean-
1009 Jacques Correia, Patrick RAbou, and Laurent Jocu. 2018. "SHADOWS : A Spectro-
1010 Gonio Radiometer for Bidirectional Reflectance Studies of Dark Meteorites and
1011 Terrestrial Analogs . Design , Calibrations , and Performances on Challenging
1012 Surfaces." *Applied Optics* 57 (29): 8279–8296.
1013 <https://doi.org/https://doi.org/10.1364/AO.57.008279>.
- 1014 Ray, Dwijesh, and Anil D. Shukla. 2018. "The Mukundpura Meteorite, a New Fall of CM
1015 Chondrite." *Planetary and Space Science* 151: 149–54.
1016 <https://doi.org/10.1016/j.pss.2017.11.005>.
- 1017 Reddy, V., T. L. Dunn, C. A. Thomas, N. A. Moskovitz, and T. H. Burbine. 2015. "Mineralogy
1018 and Surface Composition of Asteroids." *Asteroids IV*, no. 2867.
1019 https://doi.org/10.2458/azu_uapress_9780816532131-ch003.
- 1020 Rivkin, A S, E S Howell, F Vilas, and L A Lebofsky. 2002. "Hydrated Minerals on Asteroids:
1021 The Astronomical Record." In *Asteroids III*, 235–53.
1022 <https://doi.org/10.1086/300495>.
- 1023 Rivkin, Andrew S., and F. E. DeMeo. 2018. "How Many Hydrated NEOs Are There?"
1024 *Journal of Geophysical Research: Planets* 123 (December): (accepted).
1025 <https://doi.org/10.1029/2018JE005584>.
- 1026 Sanchez, Juan A., Vishnu Reddy, Andreas Nathues, Edward A. Cloutis, Paul Mann, and

- 1027 Harald Hiesinger. 2012. "Phase Reddening on Near-Earth Asteroids: Implications
1028 for Mineralogical Analysis, Space Weathering and Taxonomic Classification." *Icarus*
1029 220 (1): 36–50. <https://doi.org/10.1016/j.icarus.2012.04.008>.
- 1030 Schorghofer, N. 2008. "Lifetime of Ice on Main Belt Asteroids." *Astrophysical Journal* 682
1031 (1): 697–705. <https://doi.org/10.1086/588633>.
- 1032 Schröder, S. E., Ye Grynko, A. Pommerol, H. U. Keller, N. Thomas, and T. L. Roush. 2014.
1033 "Laboratory Observations and Simulations of Phase Reddening." *Icarus* 239: 201–
1034 16. <https://doi.org/10.1016/j.icarus.2014.06.010>.
- 1035 Shepard, Michael K., and Paul Helfenstein. 2011. "A Laboratory Study of the Bidirectional
1036 Reflectance from Particulate Samples." *Icarus* 215 (2): 526–33.
1037 <https://doi.org/10.1016/j.icarus.2011.07.033>.
- 1038 Smith, G. 1977. "Low-Temperature Optical Studies of Metal-Metal Charge-Transfer
1039 Transitions in Various Minerals." *Canadian Mineralogist* 15: 500–507.
1040 http://rruff.info/doclib/cm/vol15/CM15_500.pdf.
- 1041 Strazzulla, Gianni, E. Dotto, R. Binzel, R. Brunetto, M. A. Barucci, A. Blanco, and V. Orfino.
1042 2005. "Spectral Alteration of the Meteorite Epinal (H5) Induced by Heavy Ion
1043 Irradiation: A Simulation of Space Weathering Effects on near-Earth Asteroids."
1044 *Icarus* 174 (1): 31–35. <https://doi.org/10.1016/j.icarus.2004.09.013>.
- 1045 Stuart, Joseph Scott, and Richard P. Binzel. 2004. "Bias-Corrected Population, Size
1046 Distribution, and Impact Hazard for the near-Earth Objects." *Icarus* 170 (2): 295–

- 1047 311. <https://doi.org/10.1016/j.icarus.2004.03.018>.
- 1048 Sunshine, Jessica M, Carle M Pieters, and Stephen F Pratt. 1990. "Deconvolution of
1049 Mineral Absorption Bands : An Improved Approach." *Journal of Geophysical*
1050 *Research* 95: 6955–66.
- 1051 Takir, Driss, and Joshua P. Emery. 2012. "Outer Main Belt Asteroids: Identification and
1052 Distribution of Four 3-Mm Spectral Groups." *Icarus* 219 (2): 641–54.
1053 <https://doi.org/10.1016/j.icarus.2012.02.022>.
- 1054 Takir, Driss, Joshua P. Emery, Harry Y. Mcsween, Charles A. Hibbitts, Roger N. Clark, Neil
1055 Pearson, and Alian Wang. 2013. "Nature and Degree of Aqueous Alteration in CM
1056 and CI Carbonaceous Chondrites." *Meteoritics and Planetary Science* 48 (9): 1618–
1057 37. <https://doi.org/10.1111/maps.12171>.
- 1058 Tomeoka, Kazushige, Harry Y Mcsween, and Peter R Buseck. 1989. "Mineralogical
1059 Alteration of CM Carbonaceous Chondrites: A Review." In *Proc. NIPR Symp. Antarct.*
1060 *Meteorites*, 2:221–34.
- 1061 Tripathi, R. P., Ambesh Dixit, and N. Bhandari. 2018. "Characterization of Mukundpura
1062 Carbonaceous Chondrite." *Current Science* 114 (1): 214–17.
1063 <https://doi.org/10.18520/cs/v114/i01/214-217>.
- 1064 Usui, Fumihiko, Sunao Hasegawa, Takafumi Ootsubo, and Takashi Onaka. 2019.
1065 "AKARI/IRC Near-Infrared Asteroid Spectroscopic Survey: AcuA-Spec." *Publ. Astron.*
1066 *Soc. Japan* 71 (0): 1–41. <https://doi.org/10.1093/pasj/xxx000>.

1067 Veverka, J, P Thomas, A Harch, B Clark, J F Bell Iii, M Malin, L A Mcfadden, S Murchie, and
1068 S E Hawkins Iii. 1997. "NEAR ' s Flyby of 253 Mathilde : Images of a C Asteroid."
1069 *Science* 278 (December 1997): 2109-14.

1070 Vilas, Faith. 1994. "A Cheaper, Faster, Better Way to Detect Water of Hydratation on
1071 Solar System Bodies." *Icarus* 111: 456-67.

1072 ———. 2008. "Spectral Characteristics of Hayabusa 2 Near-Earth Asteroid Targets
1073 162173 1999 JU3 and 2001 QC34." *Astronomical Journal* 135 (4): 1101-5.
1074 <https://doi.org/10.1088/0004-6256/135/4/1101>.

1075